

High-resolution solutions of nonlinear, advection dominated problems using a generalized finite element method

Troy Shilt ^{*}, Patrick J. O'Hara [†], and Jack J. McNamara [‡]

Traditional finite element approaches are well-known to introduce spurious oscillations when applied to advection-dominated problems. We explore alleviation of this issue from the perspective of a generalized finite element formulation, which enables stabilization through an enrichment process. The presented work uses solution-tailored enrichments for the numerical solution of the one-dimensional, unsteady Burgers' equation. Mainly, generalizable exponential and hyperbolic tangent enrichments effectively capture local, steep boundary layer/shock features. Results show natural alleviation of oscillations and return smooth numerical solutions over coarse grids. Additionally, significantly improved error levels are observed compared to Lagrangian finite element methods.

Keywords: GFEM, XFEM, Burgers' equation, advection-diffusion

Nomenclature

\mathbf{A}	= matrix containing asymmetric terms
$E_{\alpha j}$	= the j th enrichment function defined over node α
\mathbf{f}_{Γ_N}	= RHS vector corresponding to Neumann boundary condition terms
g_{Γ_D}	= Dirichlet boundary conditions
g_{Γ_N}	= Neumann boundary conditions
h	= element size
H^1	= first order Hilbert space
\tilde{H}^1	= subset of H^1 satisfying prescribed Dirichlet boundary conditions g_{Γ_D}
\hat{H}^1	= subset of H^1 which vanish on the Dirichlet boundary Γ_D
\mathbf{K}	= stiffness matrix
m_α	= dimension of the space χ_α
\mathbf{M}	= mass matrix
$N(h)$	= total number of nodes in domain Ω , determined by h
Pe	= Péclet number
\mathbb{R}^n	= n -dimensional real space
S^{GFEM}	= GFEM trial space
t_b	= Breaking time / time when a shock first forms in the inviscid Burgers' equation
u	= test/solution field
u_h	= FEM/GFEM approximation
u_{IC}	= initial condition
\tilde{V}	= finite-dimensional subspace of \tilde{H}^1
\hat{V}	= finite-dimensional subspace of \hat{H}^1
w	= trial/weighting functions
w_h	= FEM/GFEM trial/weighting functions
\mathbf{x}_α	= point over which patch ω_α is defined
α	= node in the computational domain
Γ	= computational domain boundary
Γ_D	= domain boundary where Dirichlet boundary conditions are prescribed

^{*}PhD candidate, shilt.4@osu.edu, Department of Mechanical and Aerospace Engineering. The Ohio State University, Columbus, OH, 43210, USA

[†]Research Engineer, Air Force Research Laboratory, Wright-Patterson AFB, OH, 45433, USA

[‡]Professor, mcnamara.190@osu.edu, Department of Mechanical and Aerospace Engineering. The Ohio State University, Columbus, OH, 43210, USA

Γ_N	= domain boundary where Neumann boundary conditions are prescribed
ν	= kinematic viscosity / diffusion coefficient
$\phi_{\alpha j}$	= the j th GFEM shape function corresponding to node α
φ_α	= finite element shape function over node α
χ_α	= local approximate space / space of enrichment functions
ω_α	= patch defined over node α
Ω	= computational domain
\emptyset	= null set

I. Introduction

There is an increased interest in applying finite element methods (FEM) to fluid dynamic problems due to a desire to obtain computationally efficient solutions of multiscale flows. Generalized/extended finite element methods (G/XFEM) are a promising approach towards this goal due to a high degree of flexibility for incorporating solution-tailored features into the finite element approximation space while maintaining local solution conformity [1–5]. It has been noted in Gracie et al. [6] that the G/XFEM are equivalent approaches, and for the rest of the paper, the authors will adopt the use of the term GFEM to refer to both methods. Previous work by the authors has explored the application of GFEM to different aspects of solving fluid dynamics problems. For example, in [7] it is shown that properties of the GFEM naturally mitigate the effect of locking in Stokes flow, a regime where viscous forces are dominant. The authors also previously explored mitigation of spurious oscillations using GFEM for the linear advection-diffusion equation in [8]. Here insights are provided on the natural capability of the enrichment process for stabilizing advection-dominated problems. Additionally, unlike traditional stabilized methods (streamline upwind/Petrov-Galerkin method [9], Galerkin/least-squares [10, 11], residual-free bubble methods [12, 13]), no restrictions are placed on the enrichment selection process, thus allowing the choice of solution-tailored enrichments that enable stable, high-accuracy solutions.

This paper extends our previous work on the advection-diffusion equation and explores solution-tailored enrichments applied to the one-dimensional, unsteady Burgers’ equation. The viscous Burgers’ equation is identical to the advection-diffusion equation, except the advection coefficient is replaced by the solution variable, u , thus resulting in a nonlinear term. This equation was first introduced by Bateman in [14] as a relatively simple equation to explore discontinuous solutions as the kinematic viscosity tends towards zero. It was not until many years later that Burgers explored this equation in [15] as a nonlinear equation with similar phenomena to turbulence. Nowadays, the Burgers’ equation is known to have physical relevance for problems which include: viscous flows, shock theory, gas dynamics, cosmology, traffic flow, and quantum computing [16]. The Burgers’ equation has many features similar to the Navier-Stokes equations and is used to clarify the interaction between transient, dissipative, and nonlinear advective terms. Specifically, the Burgers’ equation contains an inertial and dissipation range similar to turbulence in the Navier-Stokes equations [17, 18]. As such, numerical simulation of the Burgers’ equation presents a challenge when inertial effects dominate the solution, analogous to challenges associated with numerically solving Navier-Stokes equations with high Reynolds numbers. These highly advective problems often demand ultra-fine discretizations to resolve the system’s multiscale behavior accurately; otherwise, spurious oscillations arise in the numerical solution.

The remaining outline of this paper is as follows: first, we discuss the governing equations for the viscous Burgers’ equation, formulation of the GFEM nonlinear system of equations, and linearization using Newton-Raphson. Next, the inviscid Burgers’ equation is presented, followed by a discussion on the formation of shocks in the domain and numerical stability. Finally, we present numerical examples for the GFEM solution to the unsteady one-dimensional Burgers’ equation, along with a general discussion of the results.

II. Viscous Burgers’ equation

A. Preliminaries

Let Ω be an open set contained in \mathbb{R}^n , $n \geq 1$, with a piecewise smooth boundary Γ . Vector and tensor fields defined on Ω are in boldface notation with lowercase and uppercase variables, respectively (e.g., vector \mathbf{y} and tensor \mathbf{A}). For prescribing boundary conditions, it is necessary to define $\Gamma = \Gamma_D \cup \Gamma_N$ such that $\Gamma_D \cap \Gamma_N = \emptyset$, where Γ_D denotes part of the boundary for prescribed Dirichlet boundary conditions, and Γ_N denotes part of the boundary for prescribed Neumann boundary conditions.

B. Governing equation

The one-dimensional viscous Burgers' equation is the following: find u such that

$$\begin{aligned} \frac{\partial u}{\partial t} + u \frac{\partial u}{\partial x} - \nu \frac{\partial^2 u}{\partial x^2} &= 0 \quad \text{on } \Omega \\ u(x, 0) &= u_{IC}(x) \quad \text{on } \Omega \\ u(x, t) &= g_{\Gamma_D}(x, t) \quad \text{on } \Gamma_D \\ \frac{\partial u(x, t)}{\partial x} &= g_{\Gamma_N}(x, t) \quad \text{on } \Gamma_N \end{aligned} \quad (1)$$

where when referring to fluids, ν is the kinematic viscosity, and $u(x, t)$ is the fluid velocity. The weak formulation of the boundary value problem, Eq.1, is obtained by multiplying by weighting functions w and integrating over the domain Ω . The formulation is as follows: find $u \in \tilde{H}^1$ such that for all $w \in \tilde{H}^1$:

$$\int_{\Omega} \left(w \frac{\partial u}{\partial t} + wu \frac{\partial u}{\partial x} + \nu \frac{\partial w}{\partial x} \frac{\partial u}{\partial x} \right) d\Omega = \nu \int_{\Gamma_N} w \frac{\partial u}{\partial x} d\Gamma_N \quad (2)$$

where:

$$\tilde{H}^1 = \{u \in H^1 \mid u = g_{\Gamma_D}(x, t) \text{ on } \Gamma_D\} \quad (3)$$

$$\dot{H}^1 = \{w \in H^1 \mid w = 0 \text{ on } \Gamma_D\} \quad (4)$$

Note that the above formulation does not detail enforcement of Dirichlet boundary conditions (g_{Γ_D}). This will be the focus of a later section. The Galerkin formulation is obtained by assuming finite-dimensional approximations of the test and trial functions. Let \tilde{V} be a finite-dimensional subspace of the space \tilde{H}^1 , such that $u_h \in \tilde{V}$ is a finite-dimensional approximate solution to the weak form of the boundary value problem, Eq.2, and similarly define \dot{V} to be a finite-dimensional subspace of the space \dot{H}^1 . The Galerkin formulation is as follows: find $u_h \in \tilde{V}$ such that for all $w_h \in \dot{V}$:

$$\int_{\Omega} \left(w_h \frac{\partial u_h}{\partial t} + w_h u_h \frac{\partial u_h}{\partial x} + \nu \frac{\partial w_h}{\partial x} \frac{\partial u_h}{\partial x} \right) d\Omega = \nu \int_{\Gamma_N} w_h \frac{\partial u_h}{\partial x} d\Gamma_N \quad (5)$$

C. GFEM approximation space

Constructing the GFEM approximation space consists of three components: a) patches, b) a partition of unity, and c) local approximation spaces.

a) *Patches*: build an open covering defined such that for a parameter $h > 0$:

$$\Omega \subset \bigcup_{\alpha=1}^{N(h)} \omega_{\alpha} \quad (6)$$

where ω_{α} are patches defined over \mathbf{x}_{α} , $\alpha = 1, \dots, N(h)$. Any $\mathbf{x} \in \Omega$ belongs to at most $M \leq N(h)$ elements of the set $\{\omega_{\alpha}\}_{\alpha=1}^{N(h)}$. In (G)FEM, ω_{α} is given by the union of finite elements sharing node α of the finite element mesh covering Ω . Additionally, $N(h)$ is defined to be the total number of nodes in the domain Ω . Fig. 1 provides a visual representation of patches typically used in (G)FEM for a one-dimensional domain.

b) *Partition of unity*: let $\{\varphi_{\alpha}\}_{\alpha=1}^{N(h)}$ be piecewise C^0 functions defined on Ω satisfying:

$$\sum_{\alpha=1}^{N(h)} \varphi(\mathbf{x}) = 1, \quad \forall \mathbf{x} \in \Omega \quad (7)$$

Then the set $\{\varphi_{\alpha}\}_{\alpha=1}^{N(h)}$ forms a partition of unity with respect to the open cover set $\{\omega_{\alpha}\}_{\alpha=1}^{N(h)}$. In GFEM, the set $\{\varphi_{\alpha}\}_{\alpha=1}^{N(h)}$ is typically chosen as linear, Lagrangian shape functions (see Fig. 1).

c) *Local and approximation spaces*: For each patch ω_{α} we associate an m_{α} -dimensional space $\chi_{\alpha}(\omega_{\alpha})$ of functions, denoted the local approximate space, such that:

$$\chi_\alpha = \text{span}\{E_{\alpha j}, 1 \leq j \leq m_\alpha, E_{\alpha j} \in H^1\} \quad (8)$$

where the functions $E_{\alpha j} \in \chi_\alpha$ are known as *enrichment functions*. It is assumed each χ_α contain a constant function. This inclusion allows for the set $\{\varphi_\alpha\}_{\alpha=1}^{N(h)}$ to be contained in the trial space.

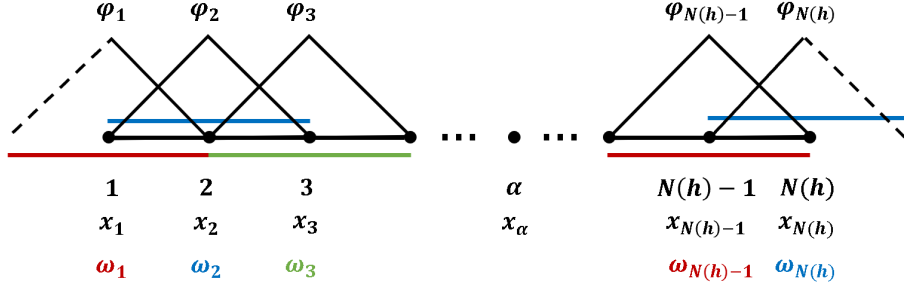


Fig. 1 Patches (ω_α) and the partition of unity composed of linear, Lagrangian shape functions (φ_α) over a one-dimensional, uniformly discretized computational domain (Ω)

Finally, the GFEM approximation space is given by:

$$S^{GFEM}(\Omega) = \text{span}\{\phi_{\alpha j} = \varphi_\alpha E_{\alpha j} \text{ (no sum over } \alpha), 1 \leq \alpha \leq N(h), 1 \leq j \leq m_\alpha\} \quad (9)$$

where $\phi_{\alpha j}$ are called the *GFEM shape functions*.

D. Solution of the GFEM system of equations

Any trial function $u_h \in S^{GFEM} \subset \tilde{V}$ may be written in vector notation as:

$$u_h = \boldsymbol{\phi}^T(x) \mathbf{c}(t) \quad (10)$$

where $\boldsymbol{\phi}$ is the vector of GFEM shape functions ($\phi_{\alpha j}$) and \mathbf{c} is the vector of corresponding weighting coefficients. GFEM test functions w_h are defined identically. Substituting Eq. 10 into the Galerkin formulation Eq. 5 results in the following system of equations:

$$\mathbf{M}\dot{\mathbf{c}}(t) = -(\mathbf{A}(t) + \mathbf{K})\mathbf{c}(t) + \mathbf{f}_{\Gamma_N}(t) \quad (11)$$

where

$$\mathbf{M} = \int_{\Omega} \boldsymbol{\phi} \boldsymbol{\phi}^T d\Omega \quad (12)$$

$$\mathbf{A}(t) = \int_{\Omega} \boldsymbol{\phi} \boldsymbol{\phi}^T \mathbf{c}(t) \frac{\partial \boldsymbol{\phi}^T}{\partial x} d\Omega \quad (13)$$

$$\mathbf{K} = \nu \int_{\Omega} \frac{\partial \boldsymbol{\phi}}{\partial x} \frac{\partial \boldsymbol{\phi}^T}{\partial x} d\Omega \quad (14)$$

$$\mathbf{f}_{\Gamma_N}(t) = \int_{\Gamma_N} \boldsymbol{\phi} g_{\Gamma_N}(x, t) d\Gamma_N \quad (15)$$

1. Time discretization using Crank-Nicolson method

The Crank-Nicolson scheme is used for temporal discretization of Eq. 11, such that:

$$2\mathbf{M} \left(\frac{\mathbf{c}^{n+1} - \mathbf{c}^n}{\Delta t} \right) = \left[\mathbf{f}_{\Gamma_N}(t^{n+1}) - (\mathbf{A}(\mathbf{c}^{n+1}) + \mathbf{K})\mathbf{c}^{n+1} \right] + \left[\mathbf{f}_{\Gamma_N}(t^n) - (\mathbf{A}(\mathbf{c}^n) + \mathbf{K})\mathbf{c}^n \right] \quad (16)$$

which may be rearranged as:

$$\mathbf{G}(\mathbf{c}^{n+1})\mathbf{c}^{n+1} = \mathbf{g} \quad (17)$$

where $\mathbf{G}(\mathbf{c}^{n+1}) = \frac{2}{\Delta t}\mathbf{M} + \mathbf{A}(\mathbf{c}^{n+1}) + \mathbf{K}$ and $\mathbf{g} = \mathbf{f}_{\Gamma_N}(t^{n+1}) + \left[\mathbf{f}_{\Gamma_N}(t^n) - (\mathbf{A}(\mathbf{c}^n) + \mathbf{K})\mathbf{c}^n \right]$.

2. Enforcing Dirichlet boundary conditions

In the Lagrangian finite element method, the Kronecker delta property of the shape functions allows direct enforcement of Dirichlet boundary conditions by setting the coefficients equal to the desired solution values. However, additional degrees of freedom per node introduced through the GFEM enrichment process makes this approach nontrivial. A straightforward manner of enforcing desired boundary conditions in GFEM is to add a penalty term on both sides of the system of equations Eq. 17 such that:

$$[\mathbf{M}_{\Gamma_D} + \mathbf{G}(\mathbf{c}^{n+1})]\mathbf{c}^{n+1} = \mathbf{g} + \mathbf{f}_{\Gamma_D}(t) \quad (18)$$

where β is the penalty parameter that is typically very large in relation to the other matrix components, but not so large to cause ill conditioning of system matrices, and:

$$\mathbf{M}_{\Gamma_D} = \int_{\Gamma_D} \boldsymbol{\phi}\boldsymbol{\phi}^T d\Gamma_D \quad (19)$$

$$\mathbf{f}_{\Gamma_D}(t) = \int_{\Gamma_D} \boldsymbol{\phi}g_{\Gamma_D}(x, t) d\Gamma_D \quad (20)$$

3. Iteration of the nonlinear system with Newton-Raphson method

Equation 18 is a nonlinear system of equations with knowns \mathbf{c}^n and unknowns \mathbf{c}^{n+1} . Using the Newton-Raphson method, the solution may be iterated to solve for the solutions at the $n + 1$ time step. To do so, assume $\mathbf{c}^{n+1} = \mathbf{c}^n + \boldsymbol{\epsilon}$, where solutions at the previous time steps n are an approximation of the $n + 1$ solution, and $\boldsymbol{\epsilon}$ is a small correction. First, applying this above decomposition to the nonlinear matrix term ($\mathbf{A}(t^{n+1})$) product with solution coefficients at the $n + 1$ time step (\mathbf{c}^{n+1}) simplify to the following after neglecting the underlined $O(\epsilon^2)$ terms:

$$\begin{aligned} \mathbf{A}(\mathbf{c}^{n+1})\mathbf{c}^{n+1} &\approx \mathbf{A}(\mathbf{c}^n)\mathbf{c}^n + \left(\mathbf{A}(\mathbf{c}^n) + \int_{\Omega} \boldsymbol{\phi}\boldsymbol{\phi}^T \left(\frac{\partial \boldsymbol{\phi}}{\partial x} \mathbf{c}^n \right) d\Omega \right) \boldsymbol{\epsilon} + \underline{O(\epsilon^2)} \\ &\approx \mathbf{A}(\mathbf{c}^n)\mathbf{c}^n + \left(\mathbf{A}(\mathbf{c}^n) + \tilde{\mathbf{A}}(\mathbf{c}^n) \right) \boldsymbol{\epsilon} + \underline{O(\epsilon^2)} \end{aligned} \quad (21)$$

Substitution of $\mathbf{c}^{n+1} = \mathbf{c}^n + \boldsymbol{\epsilon}$ and Eq. 21 into Eq. 18 results in the following system of equations to solve for the corrections $\boldsymbol{\epsilon}$:

$$\tilde{\mathbf{G}}\boldsymbol{\epsilon} = \tilde{\mathbf{g}} \quad (22)$$

where $\tilde{\mathbf{G}} = \mathbf{G}(\mathbf{c}^n) + \tilde{\mathbf{A}}(\mathbf{c}^n) + \mathbf{M}_{\Gamma_D}$ and $\tilde{\mathbf{g}} = \mathbf{g} + \mathbf{f}_{\Gamma_D} - (\mathbf{G}(\mathbf{c}^n) + \mathbf{M}_{\Gamma_D})\mathbf{c}^n$. Finally, iterate over Eq. 22 until some residual is converged.

4. Linear solver

Note that due to the ill-conditioning of the GFEM formulation (see [19]) the iterative algorithm presented in [2] and displayed in Algo. 1 is used to solve the potentially indefinite system of equations. For subsequent numerical examples

$\epsilon_1 = \epsilon_2 = 10^{-10}$ is used.

Algorithm 1: Solution to the system of equations $\tilde{\mathbf{A}}\tilde{\mathbf{c}} = \tilde{\mathbf{b}}$

INPUT: $\tilde{\mathbf{A}}, \tilde{\mathbf{b}}$, perturbation $\epsilon_1 \ll 1$, and criterion $\epsilon_2 \ll 1$

OUTPUT: $\mathbf{c} = \mathbf{c}_i$

Initialization:

Precondition $\tilde{\mathbf{A}}\tilde{\mathbf{c}} = \tilde{\mathbf{b}}$ to equivalent system $\mathbf{A}\mathbf{c} = \mathbf{b}$ by defining:

$$T_{ij} = \frac{\delta_{ij}}{\sqrt{\tilde{\Lambda}_{ij}}}$$

$$\mathbf{A} = \mathbf{T}\tilde{\mathbf{A}}\mathbf{T}$$

$$\mathbf{c} = \mathbf{T}^{-1}\tilde{\mathbf{c}}$$

$$\mathbf{b} = \mathbf{T}\tilde{\mathbf{b}}$$

Perturbed matrix: $\mathbf{A}_\epsilon = \mathbf{A} + \epsilon_1 \mathbf{I}$;

Approximate system of equations solution vector: $\mathbf{c}_0 = \mathbf{A}_\epsilon^{-1}\mathbf{b}$;

Residual error of approximate system of equations: $\mathbf{r}_0 = \mathbf{b} - \mathbf{A}\mathbf{c}_0$;

Residual error of solution vector: $\mathbf{e}_0 = \mathbf{c} - \mathbf{c}_0 \approx \mathbf{A}_\epsilon^{-1}\mathbf{r}_0$;

while $\left| \frac{e_i A e_i}{c_i A c_i} \right| > \epsilon_2$ **do**

$$\begin{cases} \mathbf{r}_i = \mathbf{r}_{i-1} - \sum_{j=0}^{i-1} \mathbf{A}\mathbf{e}_j; \\ \mathbf{e}_i = \mathbf{A}_\epsilon^{-1}\mathbf{r}_i; \\ \mathbf{c}_i = \mathbf{c}_0 + \sum_{j=0}^{i-1} \mathbf{e}_j; \end{cases}$$

end

return $\tilde{\mathbf{c}} = \mathbf{T}\mathbf{c}_i$

5. Initial condition

Solution of Eq. 22 requires an initial solution vector, \mathbf{c}^0 , which approximates the initial value problem $u_h(x, 0) = \phi^T(x)\mathbf{c}^0 \approx u_{IC}(x)$. The initial solution vector is obtained by solving the Galerkin formulation of this IVP, such that:

$$\mathbf{M}\mathbf{c}^0 = \int_{\Omega} \phi u_{IC}(x) d\Omega. \quad (23)$$

III. Inviscid Burgers' Equation

A. Governing equation

The inviscid Burgers' equation represents a limiting case where the kinematic viscosity tends toward zero ($\nu \rightarrow 0$). The resulting inviscid Burgers' equation is the following: find u such that:

$$\begin{aligned} \frac{\partial u}{\partial t} + u \frac{\partial u}{\partial x} &= 0 \quad \text{on } \Omega \\ u(x, 0) &= u_{IC}(x) \quad \text{on } \Omega \\ u(x, t) &= g_{\Gamma_D}(t) \quad \text{on } \Gamma_D \\ \frac{\partial u(x, t)}{\partial x} &= g_{\Gamma_N}(t) \quad \text{on } \Gamma_N \end{aligned} \quad (24)$$

Using the method of characteristics an implicit solution to Eq. 24 can be constructed. Readers are directed to [20] for additional details on this procedure. The resulting implicit solution is given by $u(x, t) = u_{IC}(x - ut) = u_{IC}(\xi)$, with a characteristic trajectory $x = ut + \xi$, where ξ is an arbitrary point on the x -axis of the x - t plane. Note the formulation of the GFEM system of equations for this inviscid case is identical to that of Eq. 11 with \mathbf{K} removed.

B. Formation of shocks

In the inviscid case, a discontinuity ("shock") will form in the domain if $u'_{IC}(x) < 0$. This work's notion of a shock is assumed to be inclusive of any solution which contains a steep gradient. Therefore, the distinction between the

inviscid and viscous Burgers' equation for shock formation is the discontinuity that appears in the domain. Additionally, the time when the discontinuity first occurs is denoted the breaking time and is given by:

$$t_b = \frac{-1}{\min u'_{IC}(x)} \quad (25)$$

If $u_{IC}(x)$ crosses the x -axis at x_b , such that $u_{IC}(x_b) = 0$ and $u'_{IC}(x_b) < 0$, the shock that forms will be stationary at x_b . In the case where $u'_{IC}(x) < 0$ and $u_{IC}(x)$ does *not* cross the x -axis, the shock formed will be moving. If $u_{IC}(x) > 0$ the shock will travel in the positive x -direction with time, otherwise for $u_{IC}(x) < 0$ the shock will travel in the negative x -direction with time. This may be demonstrated by considering a series of Riemann problems represented by the following initial conditions:

$$u_{IC}(x) = \begin{cases} b + 1 & x \leq \frac{1}{2} \\ b + 2(1 - x) & \frac{1}{2} < x < \frac{3}{2} \\ b - 1 & \frac{3}{2} \leq x \end{cases} \quad (26)$$

where b is an arbitrary value to translate the initial condition. The resulting solution to Eq. 24, with initial conditions Eq. 26 for values of $b = \{-1.25, -1, 0, 0.5, 1, 1.25\}$, is shown in Fig 2. Observe that the initial problem is strictly negative for $b = -1.25$, and the forming shock moves to the left with time. If $b = 1.25$, the initial problem is strictly positive and moves to the right. The remaining values of b cross the x -axis at some point and form a stationary wave. Addressing moving shocks is outside of the scope of this paper, as the authors are concerned with addressing stability concerns in the GFEM. Thus, this work considers only stationary shocks for subsequent numerical examples. However, the authors note that previous work on GFEM to solve time-dependent problems indicates a promise to handle transient, local behavior. The authors direct the readers to [21] for work on GFEM solution to highly localized sharp, transient thermal gradients as an example of such application.

C. A note on stability

Recall the viscous Burgers' equation (Eq. 2) is form identical to the advection-diffusion equation, where the advection coefficient is replaced by the solution variable, u . For advection-diffusion equations, the Péclet number is considered for stability of the linear FEM. Specifically, for linear FEM solution over uniform grid size, h , $Pe = \frac{ah}{2\nu} > 1$ results in spurious oscillations, where a and ν are the rate of advection and rate of diffusion, respectively. Rearranged, the required element size to eliminate spurious oscillations in the numerical solution is determined by $h \leq \frac{2\nu}{a}$. Using this, a conservative estimate for stability of the Burgers' equation is obtained by replacing a with the absolute maximum value of u at $t = 0$. Specifically, for $\max |u(x, 0)| = \max |u_{IC}(x)|$, then $h \leq \frac{2\nu}{\max |u_{IC}(x)|}$. Note in the limit $\nu \rightarrow 0$, the required grid size for a stable solution in linear FEM is unachievable.

IV. Numerical results

This section presents GFEM solutions of the one-dimensional Burgers' equation. For the following examples, please consider:

- 1) All enrichments are shift by their nodal values to retain the physical meaning of the standard FEM DOFs at each node, as well as reduce potential linear dependencies between the FEM and GFEM basis.
- 2) Special consideration is necessary to integrate the non-polynomial enrichment functions accurately. The computational cost of integrating the enrichments is trivial in the following examples since the elemental matrices are not time-dependent. Such, the following work uses a conservative number of Gaussian quadrature points for each grid refinement. For example, we use ten-point Gaussian quadrature on the most refined meshes considered (approx. $\frac{1}{80}$ element size); while we use sixty-point Gaussian quadrature for the coarsest meshes considered (approx. $\frac{1}{10}$ element size). For problems where the elemental matrices are time-dependent, evaluation of the elemental matrices at each time step using Gaussian quadrature may increase costs considerably. More efficient integration strategies may be beneficial for these problems, such as the Gauss-Laguerre quadrature for exponential functions.
- 3) *A priori* error estimates are well-known for polynomial approximation spaces: for $\Omega \subset \mathbb{R}^n$ with Lipschitz boundary, a p -degree polynomial solution converges in the L_2 and H_1 norm versus total degrees of freedom at a theoretical convergence rate of $\frac{p+1}{n}$ and $\frac{p}{n}$, respectively. However, for approximation spaces containing solution-

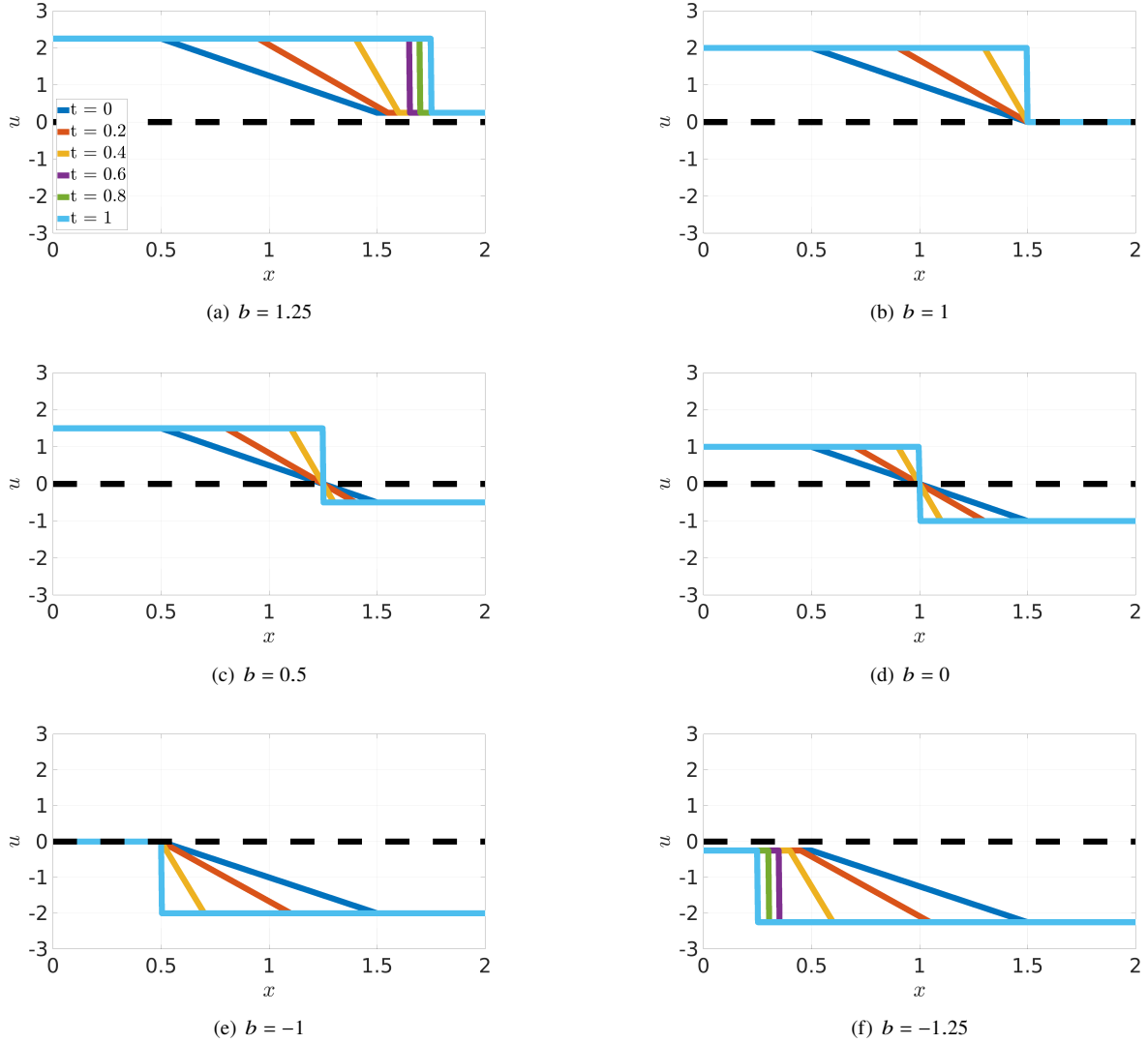


Fig. 2 Riemann solution for various initial conditions

tailored enrichments, theoretical convergence rates are not formally developed. Insights into convergence rates for solution-tailored enrichments are provided by considering convergence plots. Unless specified, convergence rates in the L_2 and H_1 norm versus total degrees of freedom use the finest two grids studied. For a sufficiently smooth solution using polynomial + non-polynomial enrichments, convergence rates are similar to those of the polynomial approximation spaces. An exception is when the numerical solution is of the same order of numerical precision as the reference solution. Same order numerical precision is often the case when using solution-tailored enrichments.

A. Numerical example 1: Boundary layer solution as the kinematic viscosity tends toward zero

1. Problem statement and reference solutions

Consider the viscous Burgers' equation (Eq. 1) defined over a unit domain ($\Omega = [0, 1]$) and subject to homogeneous Dirichlet boundary conditions everywhere ($\Gamma = \Gamma_D = 0; \Gamma_N = \emptyset$). The problem formulation is as follows: For $t \in [0, 1]$, find u such that:

$$\begin{aligned}
\frac{\partial u}{\partial t} + u \frac{\partial u}{\partial x} - \nu \frac{\partial^2 u}{\partial x^2} &= 0 \quad \text{on } \Omega \\
u(x, 0) &= \sin \pi x \quad \text{on } \Omega \\
u(0, t) = u(1, t) &= 0 \quad \text{on } \Gamma
\end{aligned} \tag{27}$$

An analytical Fourier solution to Eq. 27 is obtainable through use of the Hopf-Cole transformation, as detailed in [23]. The resulting analytical Fourier solution is:

$$u(x, t) = 2\pi\nu \frac{\sum_{n=1}^{\infty} a_n e^{-n^2 \pi^2 \nu t} n \sin n\pi x}{a_0 + \sum_{n=1}^{\infty} a_n e^{-n^2 \pi^2 \nu t} \cos n\pi x} \tag{28}$$

with Fourier coefficients, a_n :

$$\begin{aligned}
a_0 &= \int_0^1 e^{-\frac{1}{2\nu}(1-\cos \pi x)} dx \\
a_n &= 2 \int_0^1 e^{-\frac{1}{2\nu}(1-\cos \pi x)} \cos n\pi x dx
\end{aligned} \tag{29}$$

The integrals of Eq. 29 are convergent for all $\nu \neq 0$. However, for small values of ν and t , the rate of convergence of the series slows down significantly, and results in extremely difficulty computing u using this analytical expression [24]. A good discussion on this convergence issue is provided by [25] and the references within. Since this work concerns solution-tailored numerical solutions with very small viscosities, the poor accuracy of the truncated series may affect convergence rates. Thus, a 5000-element, $p = 1$ FEM solution is used as a reference instead, with the Crank-Nicolson scheme implemented with a step size of $\Delta t = \frac{1}{5000}$. For $\nu = 0$, $p = 1$ FEM is incapable of obtaining a convergent solution (recall the conservative estimate for stability $h \leq \frac{2\nu}{\max u_{IC}(x)} = 0$; or see Figs. 4 and 5). Thus, for $\nu = 0$ the analytical solution to the inviscid problem (Eq. 24) is used as a reference, and is found by solving for u in the implicit equation $u = u_{IC}(x - ut)$. Reference solutions for kinematic viscosities $\nu = \left\{ \frac{1}{10}, \frac{1}{50}, \frac{1}{100}, 0 \right\}$ are shown in Fig. 3. A boundary layer forms near $x = 1$ with thickness decreasing as ν decreases. When $\nu = 0$, a discontinuity forms at $x = 1$, starting at time $t_b = \frac{1}{\pi}$, and persisting through later times.

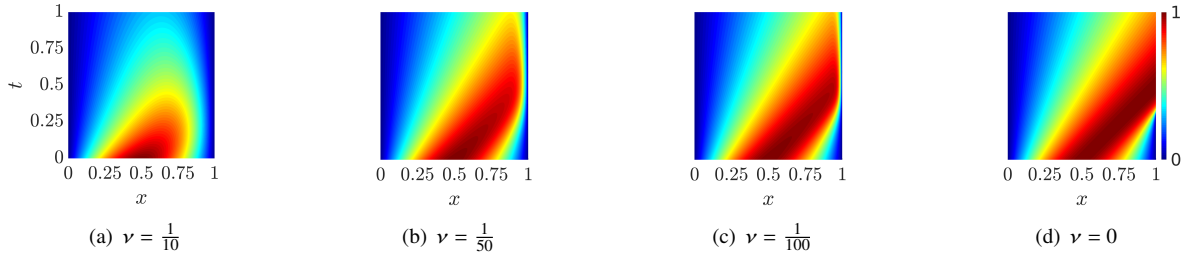


Fig. 3 Reference solution contours for the boundary layer problem over a range of ν

2. Finite element solutions

Equation 27 was initially solved over uniform grids ($h = \left\{ \frac{1}{11}, \frac{1}{23}, \frac{1}{47}, \frac{1}{95}, \frac{1}{191} \right\}$) using linear ($p = 1$) FEM. The Crank-Nicolson scheme is used for temporal discretization with a step size of $\Delta t = \frac{1}{5000}$. At each time step the Newton-Raphson method is used to iteratively solve the nonlinear set of equations. At times $t = [0, 0.25, 0.318, 0.5, 0.75, 1]$, relative L_2 and H_1 integral norms versus total degrees of freedom are shown in Figs. 4 and 5, respectively. Convergence rates are computed and presented using $h = \left\{ \frac{1}{95}, \frac{1}{191} \right\}$. It is observed as ν decreases, errors in the L_2 and H_1 norms increase. Specifically, a shift in the relative L_2 and H_1 norm is observed, with convergence rates remaining relatively unaffected except when $\nu = 0$. This is a result of the increasing difficulty in resolving the steep boundary layer that forms around $x = 1$. For $\nu = 0$, convergence does not occur once a discontinuity arises at $t_b \geq \frac{1}{\pi}$. Spurious oscillations are visually

observed in the numerical solutions for small viscosities as shown in Fig. 6, which displays 11-element solution contours. For relatively large kinematic viscosities ($\nu = \frac{1}{10}$) no oscillations are visually observed. However, when $\nu = \frac{1}{100}$ and $\nu = 0$, severe nonphysical oscillations arise in the 11-element solutions. With sufficient grid refinement, the boundary layer is captured for $\nu = \frac{1}{100}$, as exemplified by the 47-element solutions contours in Fig. 7. However grid refinement does not improve the numerical solution when $\nu = 0$.

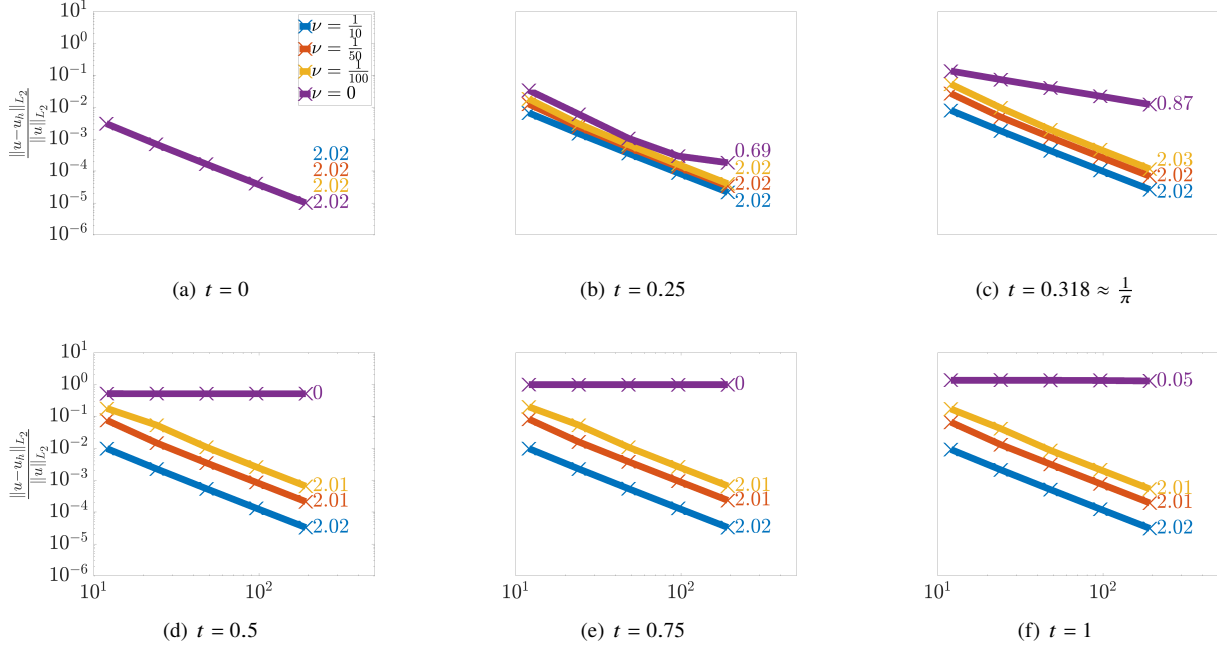


Fig. 4 $p = 1$ FEM convergence in the relative L_2 norm for the boundary layer problem at various times

3. Generalized finite element solutions

For $\nu = \frac{1}{100}$, the $p = 1$ FEM solutions are improved upon using GFEM with exponential functions as enrichments. These enrichments are applied to the local domain, $\Omega_{local} = [0.8, 1]$, roughly where the boundary layer forms. Use of these enrichments is motivated by findings in [8], which demonstrate exponential enrichments stabilize the GFEM solution around boundary layers arising in the advection-diffusion equation. Recall the Burgers' equation is of similar form to the advection-diffusion, except the rate of advection is replaced with the solution variable, u . Physically, the solution variable u may never exceed the maximum or minimum value provided by the initial conditions $u_{IC}(x)$. Thus, the specific exponential enrichment used for this problem is chosen to be $E_1 = e^{\frac{[\max u_{IC}(x)]x}{\nu}} = e^{100x}$. Results using these exponential enrichments are denoted as $p = 1 + \text{exp}$. GFEM solutions. Grid sizes, temporal discretization, and nonlinear iteration are identical to those used for the $p = 1$ FEM solutions. Convergence in the relative L_2 and H_1 integral norm at various times are shown in Figs. 8 and 9, respectively. Convergence rates are computed and presented using $h = \left\{ \frac{1}{95}, \frac{1}{191} \right\}$. Recall no theoretical convergence rates are formally developed for GFEM using the enrichments in this example. It is observed in Figs 8 and 9 that use of the exponential enrichments results in a significant reduction of error after the boundary layer forms, and at the same number of DOFs when compared to $p = 1$ FEM. Plots of the relative L_2 and H_1 integral norms versus time are shown in Fig. 10 for the 11- and 95-element GFEM solutions. The FEM and GFEM solutions have nearly identical error until $t \approx 0.25$ where boundary layer gradients become larger. The FEM solutions increase in error due to spurious oscillations, whereas the GFEM error levels remain relatively unaffected. The result is approximately 10 times reduction of error in the GFEM solutions at later time steps. Lastly, 11-element solution contours are shown in Fig. 11. Here, severe nonphysical oscillations in the $p = 1$ FEM solution are observed; whereas the $p = 1 + \text{exp}$. GFEM solution successfully captures the steep boundary layer, presenting smooth solution contours at roughly the same number of degrees of freedom.

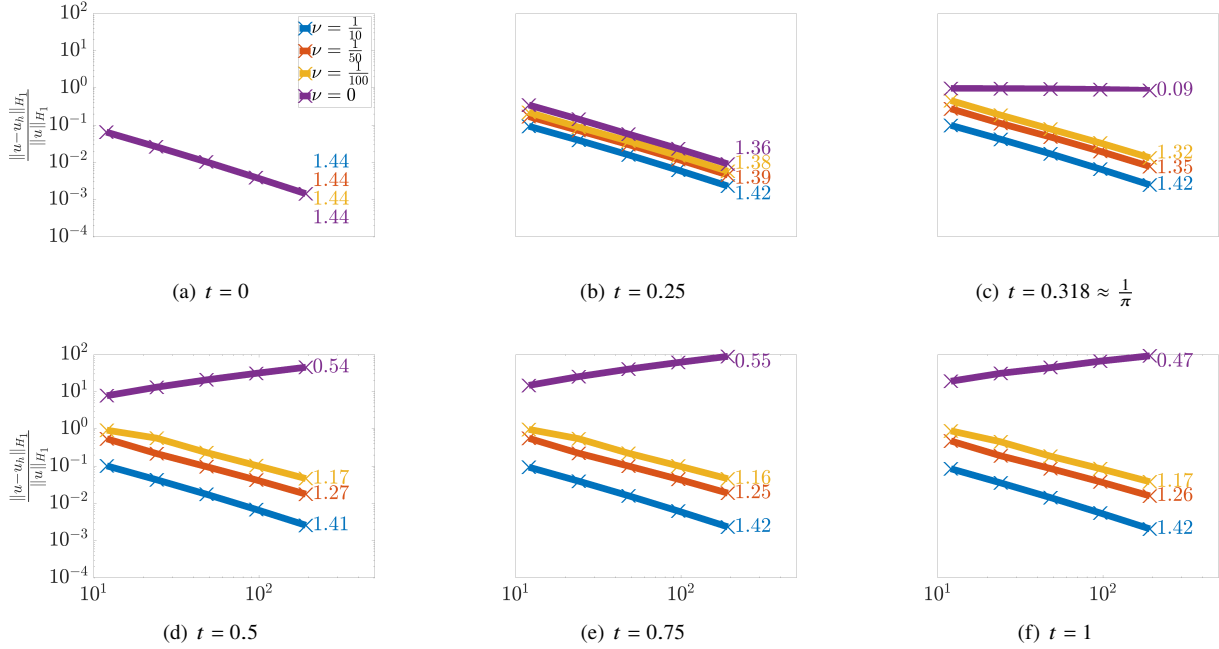


Fig. 5 $p = 1$ FEM convergence in the relative H_1 norm for the boundary layer problem at various times

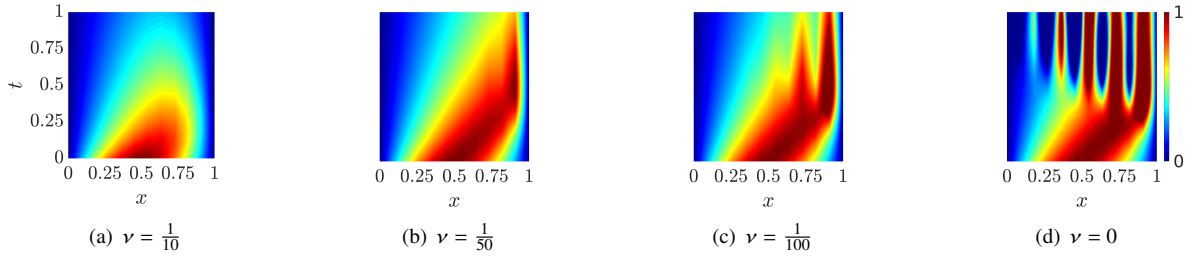


Fig. 6 11-element, $p = 1$ FEM solution contours for the boundary layer problem over a range of ν

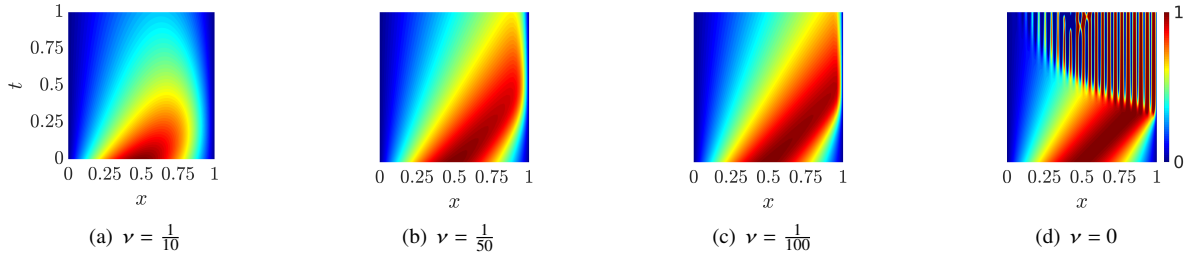


Fig. 7 47-element, $p = 1$ FEM solution contours for the boundary layer problem over a range of ν

When $\nu = 0$, the presented $p = 1$ FEM is ill-suited for two reasons: 1) enforcement of the Dirichlet boundary condition $u(1, t) = 0$ inhibits the FEM solution from capturing the discontinuity occurring at $x = 1$, and 2) increasingly steep gradients leading up to $t = \frac{1}{\pi}$ (infinitely steep at $t = \frac{1}{\pi}$) results in spurious oscillations which propagate with time. To address the first challenge, the last node in the domain at $x = 1$ is enriched with a Heaviside function which is 0 everywhere except the element containing the node. This may be thought of as a linear correction, which allows

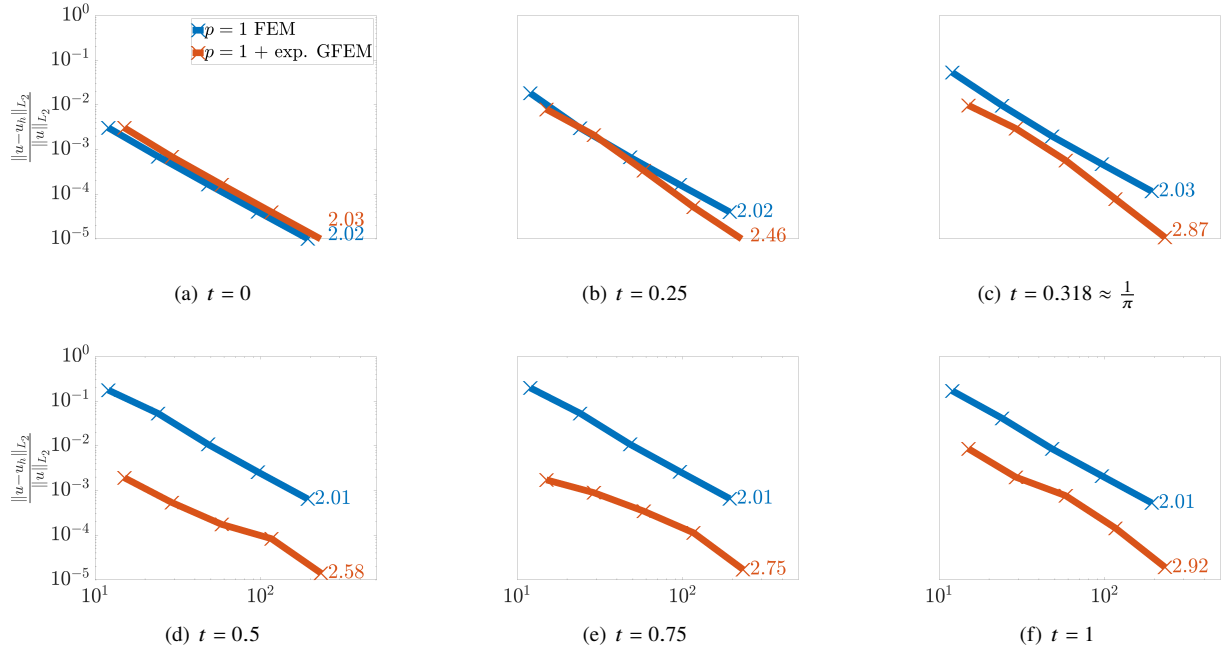


Fig. 8 Convergence in the relative L_2 integral norms for the boundary layer problem with $\nu = \frac{1}{100}$ using exponential enrichments

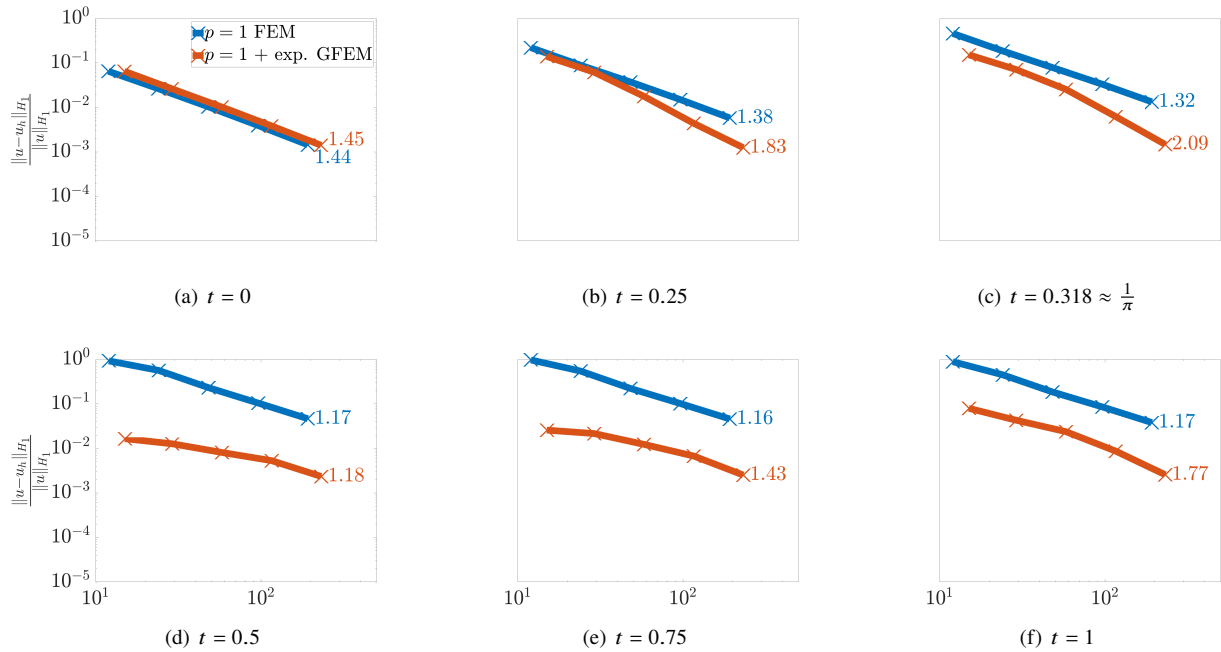


Fig. 9 Convergence in the relative H_1 integral norms for the boundary layer problem with $\nu = \frac{1}{100}$ using exponential enrichments

the GFEM to satisfy $u(1, t) = 0$, but also account for the discontinuity which arises. Results using the Heaviside enrichment are denoted as $p = 1 + \text{disc. GFEM}$ solutions. Convergence in the relative L_2 and H_1 integral norm

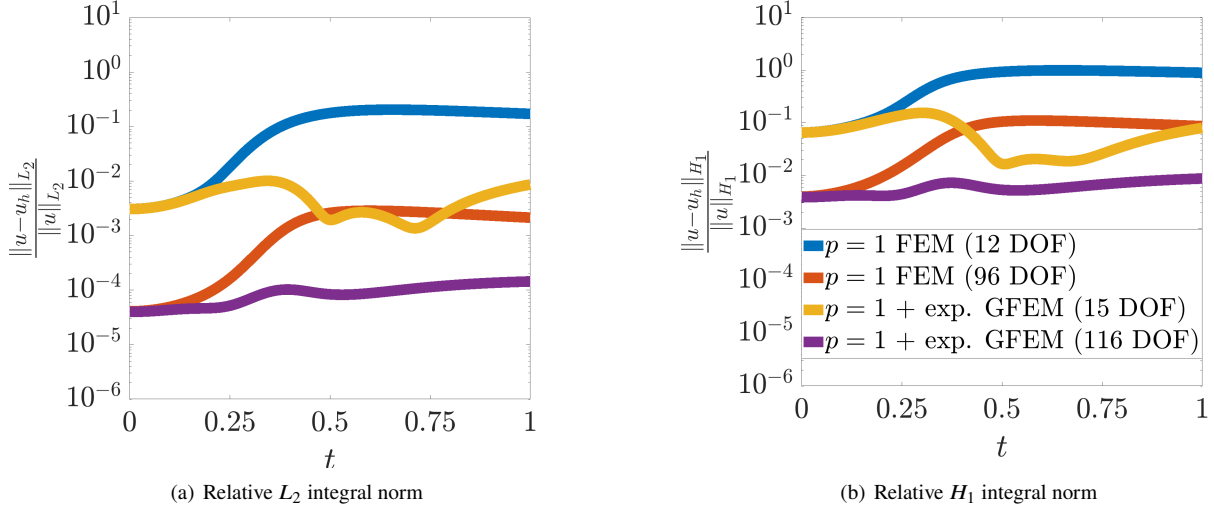


Fig. 10 Relative L_2 and H_1 integral norms versus time for 11-element and 95-element FEM and $p = 1 + \text{exp.}$ GFEM for the boundary layer problem with $\nu = \frac{1}{100}$

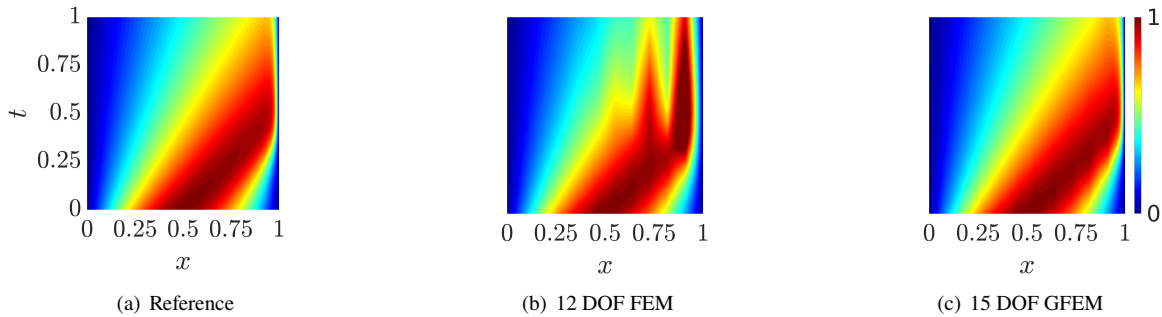


Fig. 11 11-element, $p = 1$ FEM (12 DOF) and $p = 1 + \text{exp.}$ GFEM (15 DOF) solution contours compared to the reference for the boundary layer problem with $\nu = \frac{1}{100}$

at various times are shown in Figs. 12 and 13, respectively. Convergence rates are computed and presented using $h = \left\{ \frac{1}{95}, \frac{1}{191} \right\}$. Recall no theoretical convergence rates are formally developed for GFEM using the enrichments in this example. Here convergence in the L_2 norm is significantly improved in the GFEM solutions with respect to linear FEM, however, the GFEM using Heaviside enrichment still yields poor convergence in the H_1 norm. Plots of the relative L_2 and H_1 integral norms versus time are shown in Fig. 14 for 11- and 95-element GFEM solutions. Similar to the $\nu = \frac{1}{100}$ results, the FEM and GFEM solutions have similar error levels until $t \approx \frac{1}{\pi}$ where boundary layer gradients become larger. Around $t \approx \frac{1}{\pi}$, both the FEM and GFEM solutions rise in error. This is explained as both the linear interpolation and Heaviside function are ill-suited for capturing the increasingly steep gradients leading up to the discontinuity at $t = \frac{1}{\pi}$. This is observed in Fig. 15, which provides 11-element $p = 1$ FEM and $p = 1 + \text{disc.}$ GFEM solution contours. Severe oscillations are observed in the $p = 1$ FEM solutions, whereas comparatively the GFEM solution is significantly better. However, oscillations still persist in the GFEM solutions, starting around $t = \frac{1}{\pi}$, and propagate with time. With grid refinement as shown in Fig. 16, which provides 47-element $p = 1$ FEM and $p = 1 + \text{disc.}$ GFEM solution contours, the FEM solution does not improve. However, while oscillations persist with the GFEM solution, they are significantly muted. These results demonstrate the importance of the intermediate, transitional solution features on stability of the GFEM solution for the Burgers' equation. Specific to this example, the infinitely steep boundary formed in the limit as $t \rightarrow \frac{1}{\pi}$ results in spurious oscillations even though the discontinuity is captured. To better explore the effect the

intermediate solution features have on the stability of the GFEM, a second example is examined in which a shock forms with a known steady state solution.

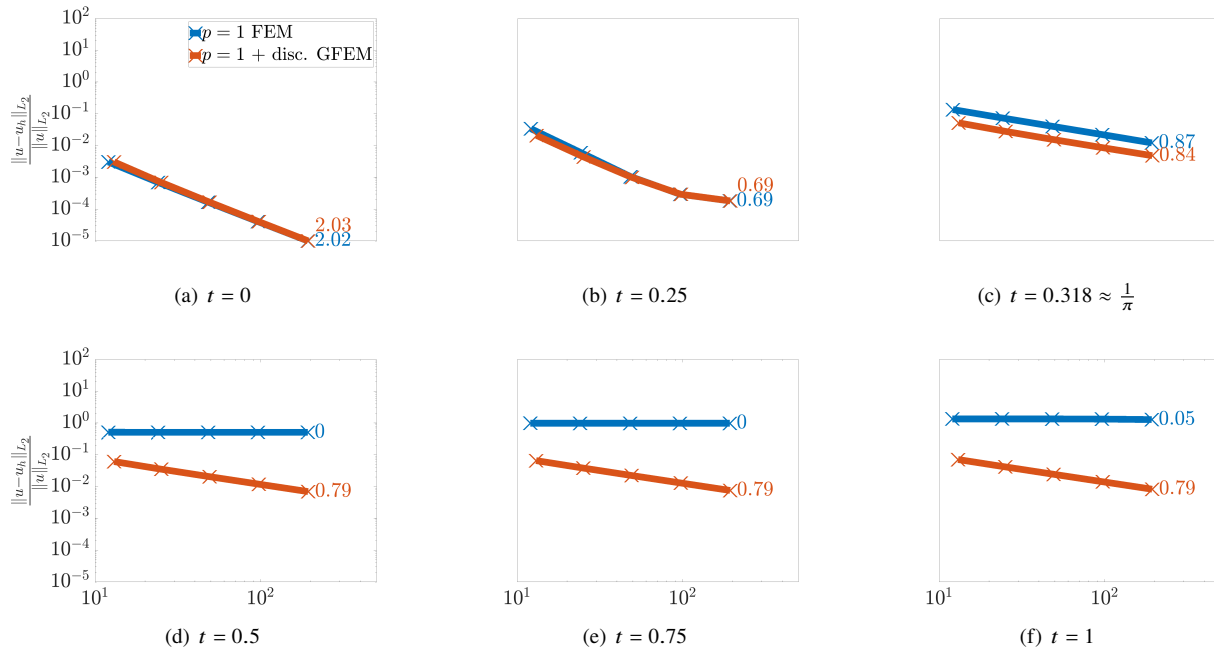


Fig. 12 Convergence in the relative L_2 integral norms for the boundary layer problem with $\nu = 0$ using Heaviside enrichments

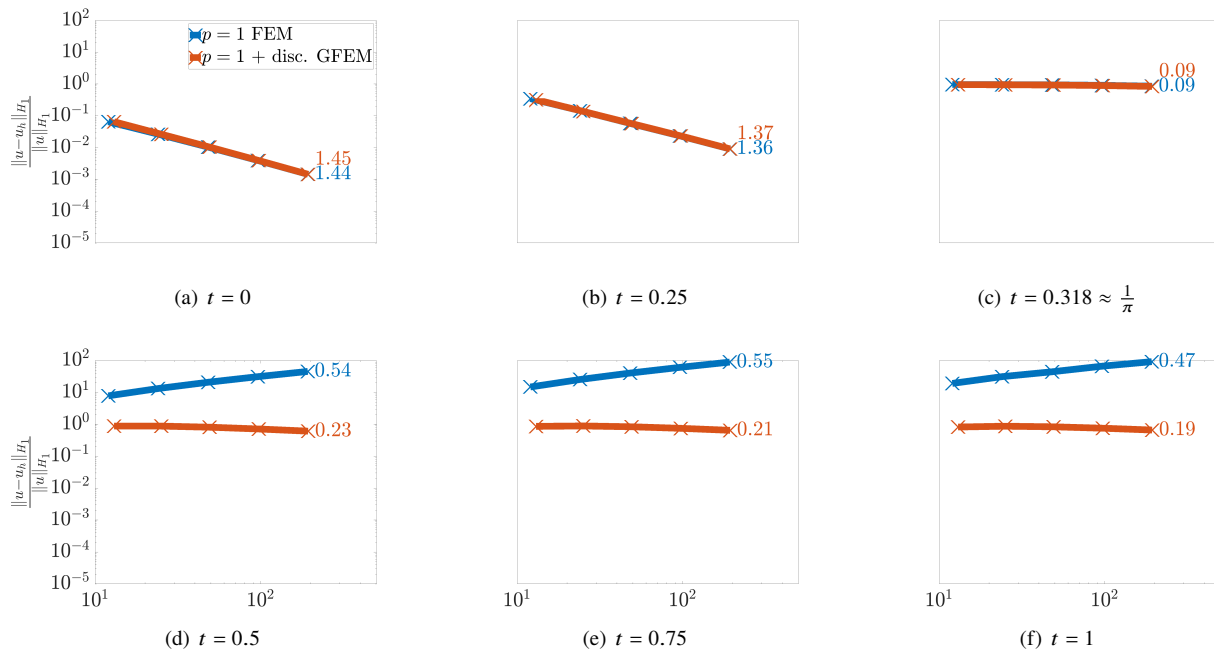


Fig. 13 Convergence in the relative H_1 integral norms for the boundary layer problem with $\nu = 0$ using Heaviside enrichments

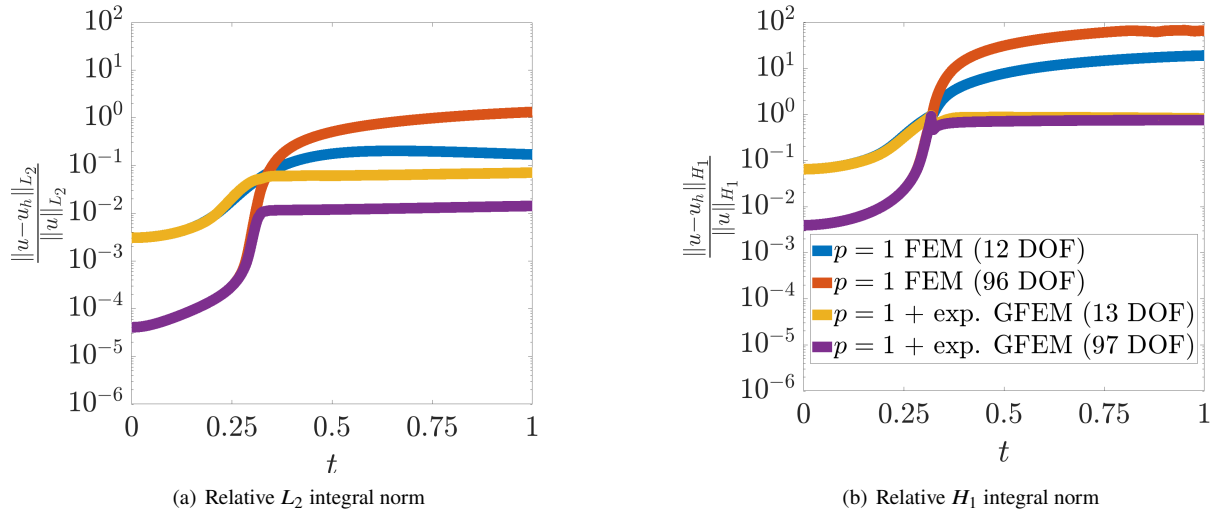


Fig. 14 Relative L_2 and H_1 integral norms versus time for 11-element and 95-element FEM and $p = 1 + \text{disc. GFEM}$ for the boundary layer problem with $\nu = 0$

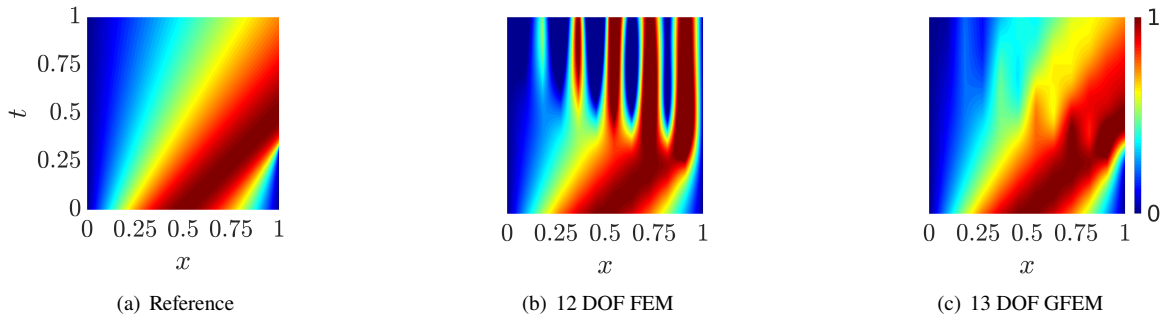


Fig. 15 11-element $p = 1$ FEM (12 DOF) $p = 1 + \text{disc. GFEM}$ (13 DOF) solution contours compared to the reference for the boundary layer problem with $\nu = 0$

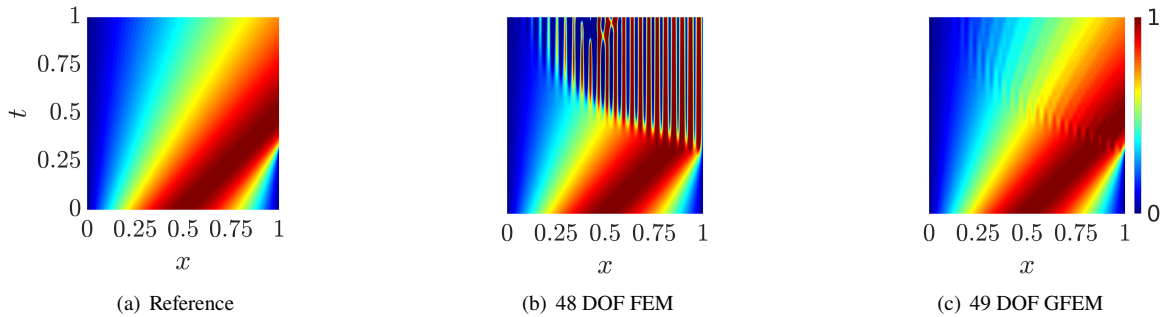


Fig. 16 47-element $p = 1$ FEM (48 DOF) $p = 1 + \text{disc. GFEM}$ (49 DOF) solution contours compared to the reference for the boundary layer problem with $\nu = 0$

B. Example 2: Shock formulation in the domain

1. Problem statement and reference solutions

Consider the viscous Burgers' equation (Eq. 1) defined over a unit domain ($\Omega = [0, 1]$) and subject to Dirichlet boundary conditions everywhere ($\Gamma = \Gamma_D$). The problem formulation is as follows: For $t \in [0, 1]$, find u such that:

$$\begin{aligned} \frac{\partial u}{\partial t} + u \frac{\partial u}{\partial x} - \nu \frac{\partial^2 u}{\partial x^2} &= 0 \quad \text{on } \Omega \\ u(x, 0) &= \cos \pi x \quad \text{on } \Omega \\ u(0, t) &= 1; u(1, t) = -1 \quad \text{on } \Gamma \end{aligned} \quad (30)$$

An analytical solution to this problem is unknown, however a steady state solution is provided by $u_{ss} = \sqrt{2k} \tanh \left[\sqrt{\frac{k}{2\nu^2}} \left(\frac{1}{2} - x \right) \right]$, where k is a constant solvable from the nonlinear equation $\sqrt{2k} \tanh \sqrt{\frac{k}{8\nu^2}} - 1 = 0$. For sufficiently small kinematic viscosity ν , the constant $k \approx \frac{1}{2}$, simplifying the steady state solution to $u_{ss} \approx \tanh \left[\frac{1}{2\nu} \left(\frac{1}{2} - x \right) \right]$. The steady state solution represents the instance when the shock has formed entirely, with the shock thickness decreasing as ν decreases. Shock location is at $x = 0.5$. The 5000-element, $p = 1$ FEM reference solution is shown in Fig. 17 for $\nu = \left[\frac{1}{50}, \frac{1}{100}, \frac{1}{500}, \frac{1}{1000} \right]$. Note the temporal term for these references were solved over $t = [0, 0.75]$ using the Crank-Nicolson scheme with a step size of $\Delta t = \frac{1}{5000}$.

2. Numerical solutions

Equation 30 was initially solved over uniform grids ($h = \left[\frac{1}{11}, \frac{1}{23}, \frac{1}{47}, \frac{1}{95}, \frac{1}{191} \right]$) using $p = 1$ FEM and GFEM enriched with the steady state solution for $\nu = \left[\frac{1}{50}, \frac{1}{100}, \frac{1}{500}, \frac{1}{1000} \right]$. The local domain the steady state enrichment is applied is given by $\Omega_{local} = \left[\frac{1}{2} - 2\nu \tanh^{-1} 0.99 - h_e, \frac{1}{2} + 2\nu \tanh^{-1} 0.99 + h_e \right]$, which includes all nodes around the shock location $x = \frac{1}{2}$ where the steady state solution $|u_{ss}| \leq 0.99$. GFEM solutions using the steady state solution as an enrichment are denoted by $p = 1 + ss$ GFEM solutions. The Crank-Nicolson scheme is used for temporal discretization with a step size of $\Delta t = \frac{1}{5000}$. At each time step the Newton-Raphson method is used to iteratively solve the nonlinear set of equations.

Plots of the relative L_2 and H_1 norm versus time are shown in Figs. 18 and 19, respectively. The $p = 1$ FEM and $p = 1 + ss$ GFEM solutions return similar error levels up until $t \approx \frac{1}{\pi}$ where shock gradients increase. This is expected since the steady state solution is not closely correlated with the initial transient solution. Around $t = \frac{1}{\pi}$, error levels rise in the $p = 1$ FEM solutions, with the rise increasing as ν becomes smaller. At $t = 0.75$, 95-element $p = 1$ FEM solutions return errors in the relative L_2 are 0.10%, 0.27%, 0.86%, and 3.3% for $\nu = \left[\frac{1}{50}, \frac{1}{100}, \frac{1}{500}, \frac{1}{1000} \right]$, respectively. Similarly in the relative H_1 norm the errors are 4.4%, 10.4%, 35.0%, and 73.5%, respectively. Use of the steady state as an enrichment in GFEM results in a significant reduction of error in both the L_2 and H_1 norm. At $t = 0.75$ the 95-element GFEM solutions enriched with the steady state solution have errors in the relative L_2 norm of 0.0027%, 0.0047%, 0.0041%, and 0.0032% for $\nu = \left[\frac{1}{50}, \frac{1}{100}, \frac{1}{500}, \frac{1}{1000} \right]$, respectively. Similarly in the relative H_1 norm the errors are 0.13%, 0.26%, 1.36%, and 2.79%, respectively. Although the $p = 1 + ss$ GFEM solutions significantly reduce relative errors with respect to $p = 1$ FEM, around $t = \frac{1}{\pi}$ errors peak to high values in both the integral norms. The peak value of the 95-element GFEM solution error in the H_1 norm for $\nu = \left[\frac{1}{50}, \frac{1}{100}, \frac{1}{500}, \frac{1}{1000} \right]$ are 0.62%, 1.3%, 12.9%, and 17.0%, respectively. These large errors arising in the GFEM solutions while the shock is forming is due to the linear interpolation and the steady state enrichment being ill-suited at capturing the intermediate solution features, similar to the results of example 1 when $\nu = 0$. Visually this is explained in Fig. 20 which shows 11-element $p = 1$ FEM and $p = 1 + ss$ GFEM solution contours. As expected for $p = 1$ FEM solutions, oscillations arise in the numerical solutions for small $\nu = \left[\frac{1}{100}, \frac{1}{500}, \frac{1}{1000} \right]$. For the $p = 1 + ss$ GFEM solutions, muted oscillations are observed for $\nu = \left[\frac{1}{500}, \frac{1}{1000} \right]$, which arise during the formation of the shock around $t = \frac{1}{\pi}$ and which propagate with time. With grid refinement as shown in Fig. 21, which provides 47-element $p = 1$ FEM and $p = 1 + ss$ GFEM solution contours, oscillations visually improve.

Convergence plots in the relative L_2 norm versus total degrees of freedom at times $t = [0, 0.25, 0.3, 0.35, 0.5, 0.75]$ for $\nu = \left[\frac{1}{50}, \frac{1}{100}, \frac{1}{500}, \frac{1}{1000} \right]$ are shown in Figs. 22 - 25, respectively. Similarly, convergence plots for the relative H_1 norm are shown in Figs. 26 - 29. Note since the steady state solution is closely correlated with the transient solution post-shock, the $p = 1 + \text{ss}$ GFEM solutions are on the same order of numerical precision as the 5000-element, $p = 1$ FEM reference solution. This is observed in the convergence plots as the $p = 1 + \text{ss}$ GFEM solution convergence begins to flatten out after around $t = \frac{1}{\pi}$. Before shock formation, both FEM and GFEM converge similarly in all norms studied. Additionally, $p = 1$ FEM performs slightly better since the steady state as an enrichment is not correlated with the initial transient solution. However, around $t = 0.25$ and persisting through $t = 0.35$, the formation of the shock results in a shift in the error, as well as sub-optimal convergence in both the FEM and GFEM solutions. After the shock has mostly formed around $t = 0.35$, error levels in the FEM solutions for the 95-element solution are larger than 30% in the H_1 norm. Error levels in the GFEM solutions at the same degrees of freedom are less than 2%. However, the effect of the oscillations which arise in the GFEM solution at earlier time steps greatly affects the convergence rate in the GFEM solution in the H_1 norm, and sub-optimal convergence is observed over all grids studied.

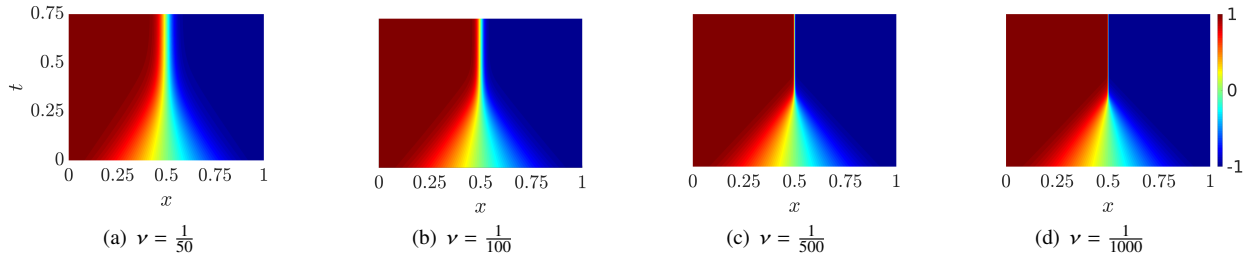


Fig. 17 5000-element FEM reference solutions for various kinematic viscosities for the shock problem

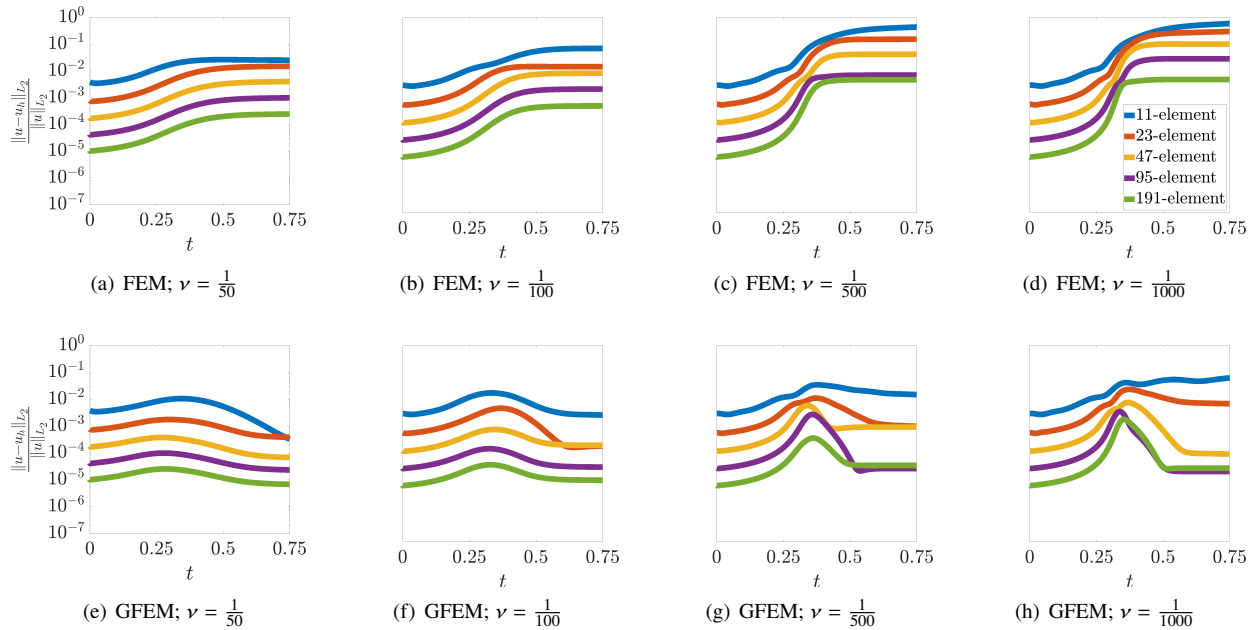


Fig. 18 Relative L_2 norm versus time for 11-, 23-, 47-, 95-element, and 191-element $p = 1$ FEM and $p = 1 + \text{ss}$ GFEM solutions over various kinematic viscosities for the shock problem

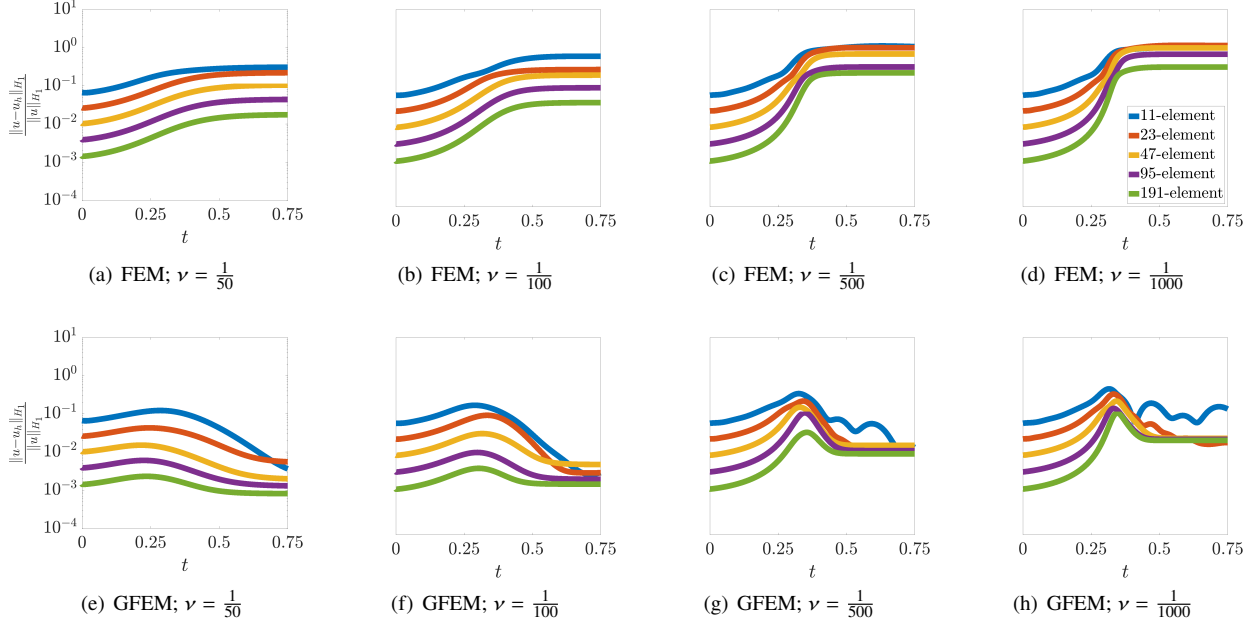


Fig. 19 Relative H_1 norm versus time for 11-, 23-, 47-, 95-element, and 191-element $p = 1$ FEM and $p = 1 + ss$ GFEM solutions over various kinematic viscosities for the shock problem

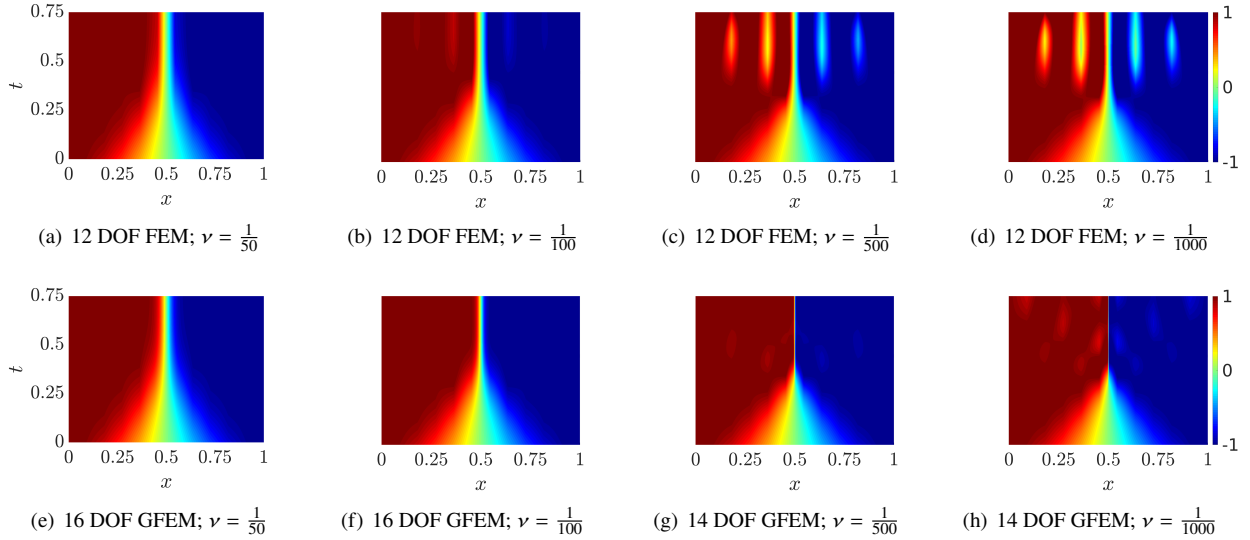


Fig. 20 11-element $p = 1$ FEM and $p = 1 + ss$ GFEM solution contours over various kinematic viscosities for the shock problem

3. Capturing intermediate solution features

For $\nu = \frac{1}{500}$, GFEM solutions are further improved during shock formation by enriching the domain with additional shock enrichments, $E_{\alpha j} = \tanh \left[\frac{1}{2\rho} \left(\frac{1}{2} - x \right) \right]$, where ρ controls the shock thickness. The local domain(s) these enrichments are applied are given by $\Omega_{local} = \left[\frac{1}{2} - 2\rho \tanh^{-1} 0.99 - h_e, \frac{1}{2} + 2\rho \tanh^{-1} 0.99 + h_e \right]$, which is the region where $|E_{\alpha j}| \leq 0.99$. Plots of the shock enrichments for various ρ are shown in Fig. 30. The $p = 1 + ss$ GFEM solution

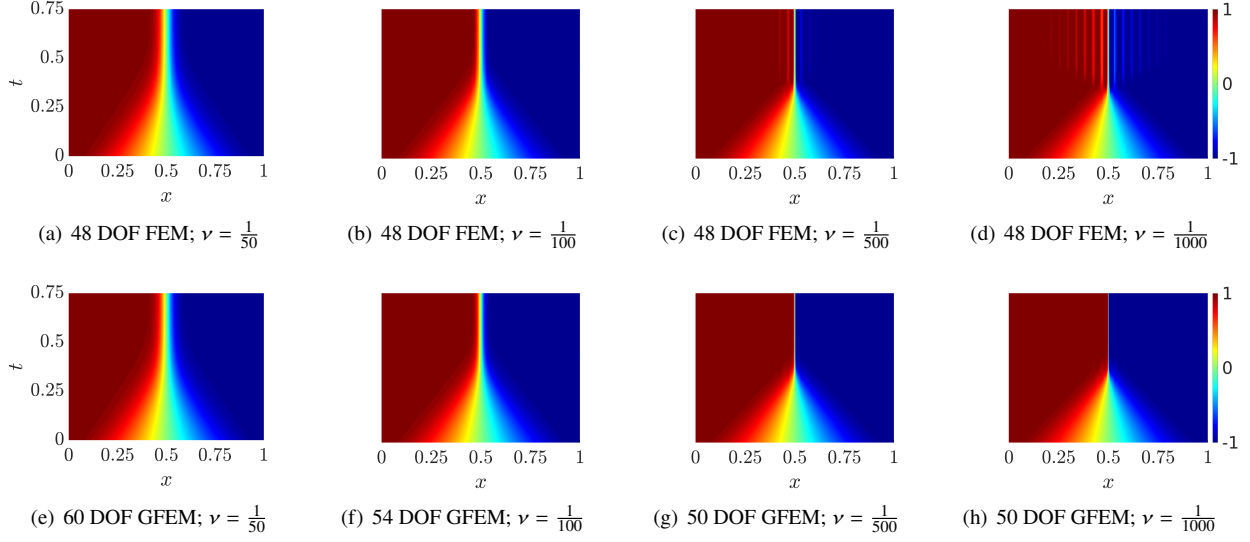


Fig. 21 47-element $p = 1$ FEM and $p = 1 + ss$ GFEM solution contours over various kinematic viscosities for the shock problem

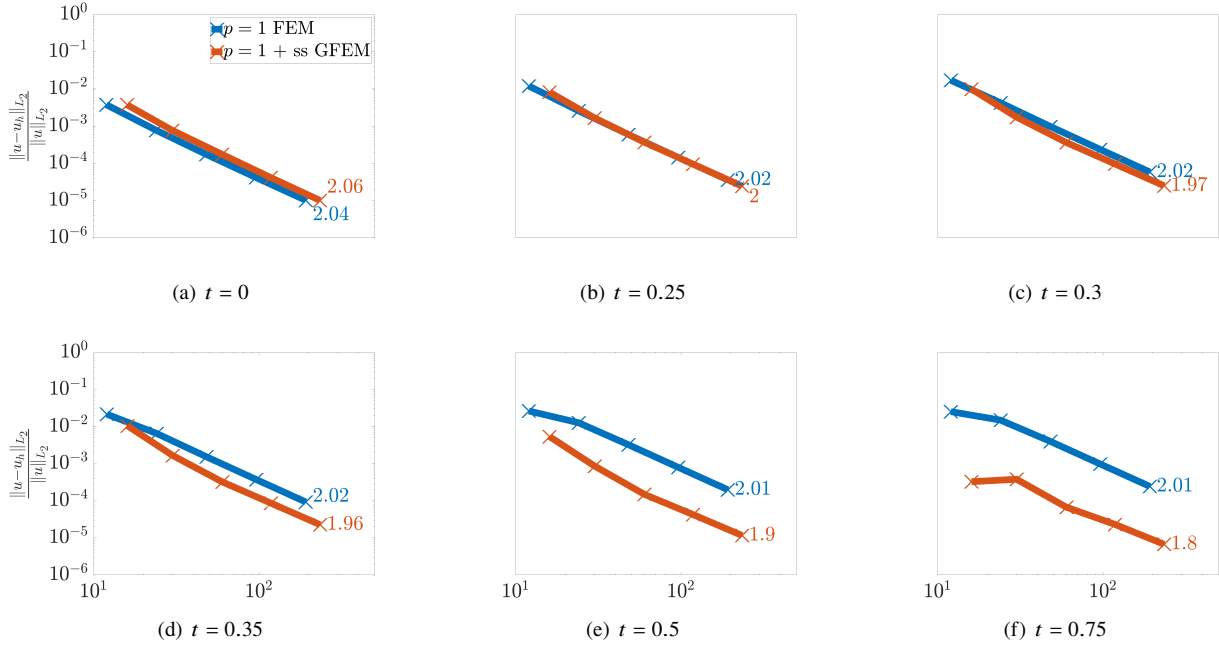


Fig. 22 Convergence the relative L_2 integral norm for the shock problem with $\nu = \frac{1}{50}$

is further enriched using $\rho = \frac{1}{50}, \rho = \frac{1}{100}, \rho = \frac{1}{200}, \rho = \left[\frac{1}{50}, \frac{1}{100}, \frac{1}{200} \right]$. These solutions are presented as $p = 1 + ss + \rho = \frac{1}{50}, p = 1 + ss + \rho = \frac{1}{100}, p = 1 + ss + \rho = \frac{1}{200}$, and $p = 1 + ss + \rho =$ all GFEM solutions, respectively. Relative L_2 and H_1 norm versus time plots are shown in Fig. 31. for 11-element solutions. Here the addition of various shock enrichments reduces the maximum error in the GFEM solutions, with the $p = 1 + ss + \rho =$ all GFEM providing the largest reduction of error. The maximum error in the L_2 and H_1 norm for 11-element $p = 1 + ss$ GFEM is 4% and

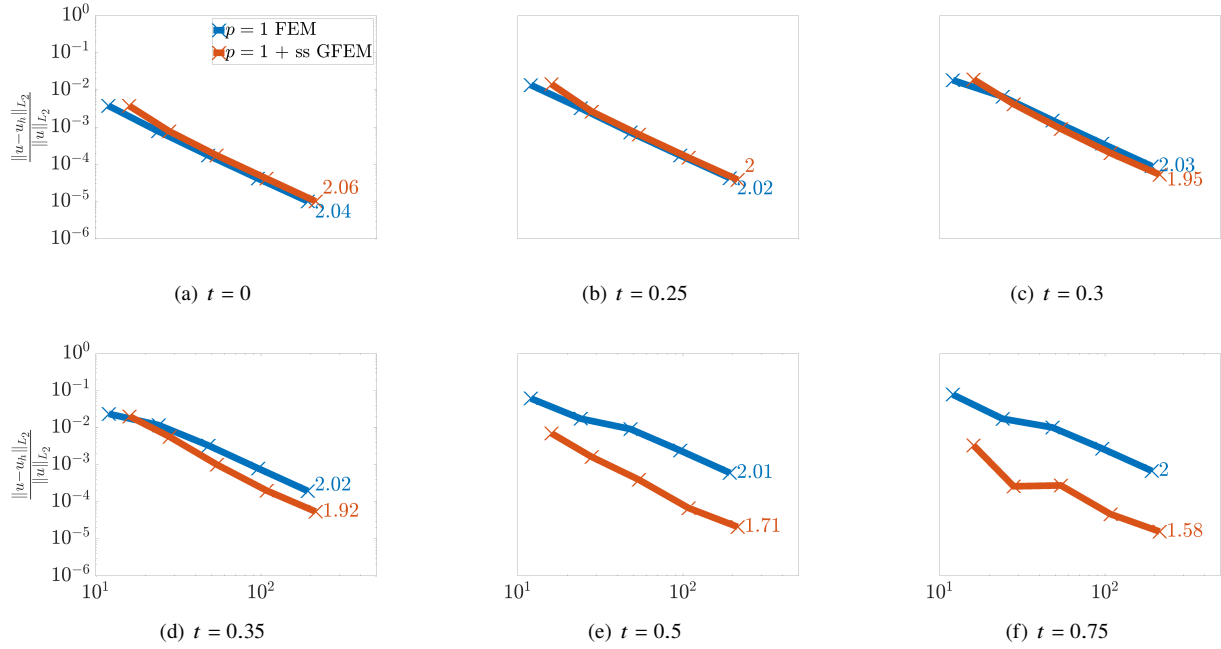


Fig. 23 Convergence the relative L_2 integral norm for the shock problem with $\nu = \frac{1}{100}$

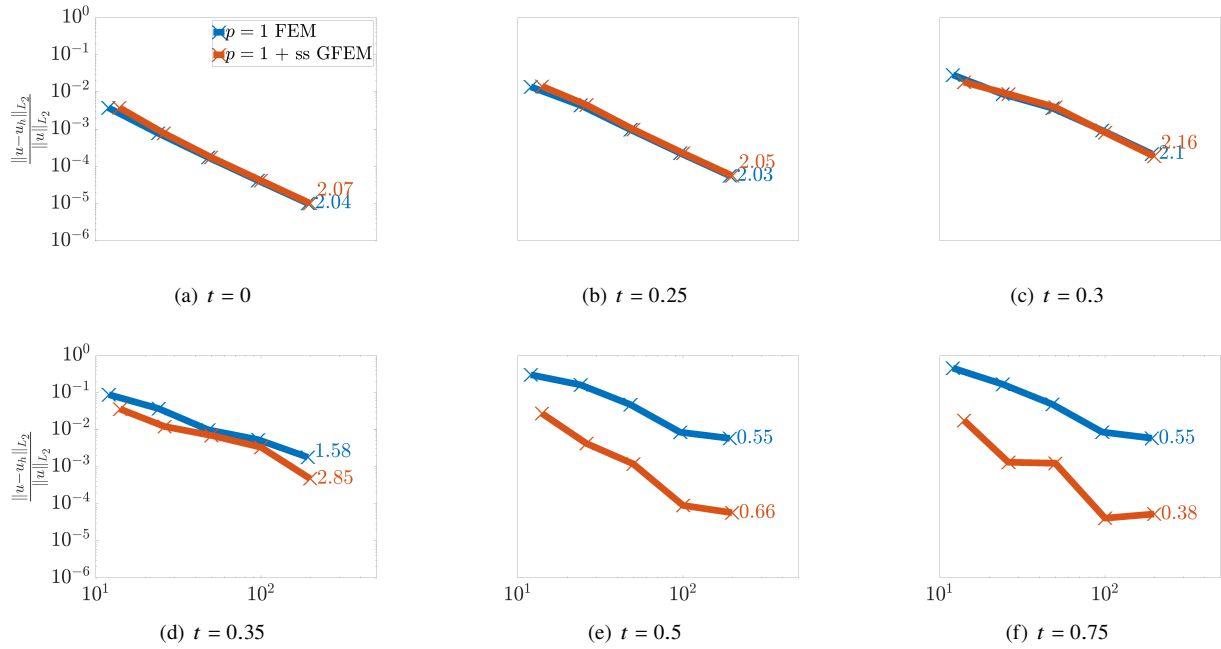


Fig. 24 Convergence the relative L_2 integral norm for the shock problem with $\nu = \frac{1}{500}$

37.9%, respectively. For 11-element $p = 1 + ss + \rho =$ all GFEM, the maximum error in the L_2 and H_1 norm is 0.75% and 9.6%, respectively, providing a 4-5 times reduction of error. Error levels improve further with grid refinement, as shown in Fig. 31 for 47-element solutions. Here, the maximum error in the L_2 and H_1 norm for 47-element $p = 1 + ss$ GFEM is 0.75% and 17.1%, respectively. For 47-element $p = 1 + ss + \rho =$ all GFEM, the maximum error in the L_2 and

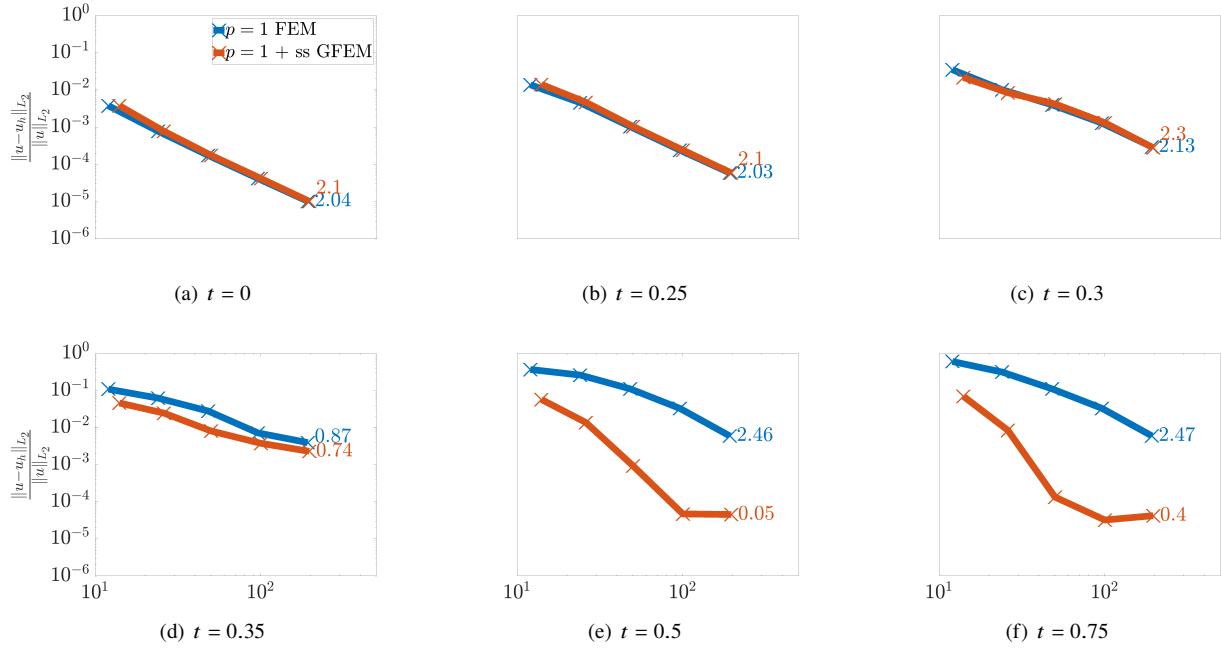


Fig. 25 Convergence the relative L_2 integral norm for the shock problem with $\nu = \frac{1}{1000}$

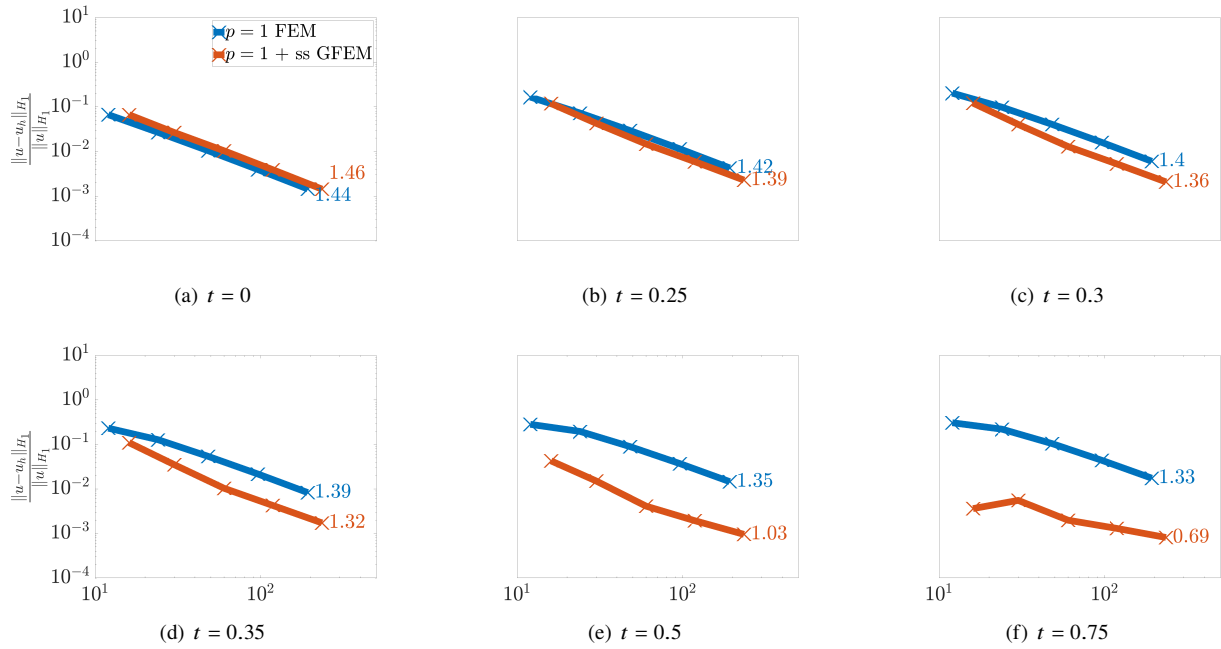


Fig. 26 Convergence the relative H_1 integral norm for the shock problem with $\nu = \frac{1}{50}$

H_1 norm is 0.031% and 1.55%, respectively, providing over a 10 times reduction of error. Lastly, convergence in the L_2 and H_1 norms versus total degrees of freedom are shown in Figs. 33 and 34, respectively. Here, the addition of multiple shock enrichments improves overall convergence, specifically during shock formation between $t = 0.25$ and $t = 0.35$.

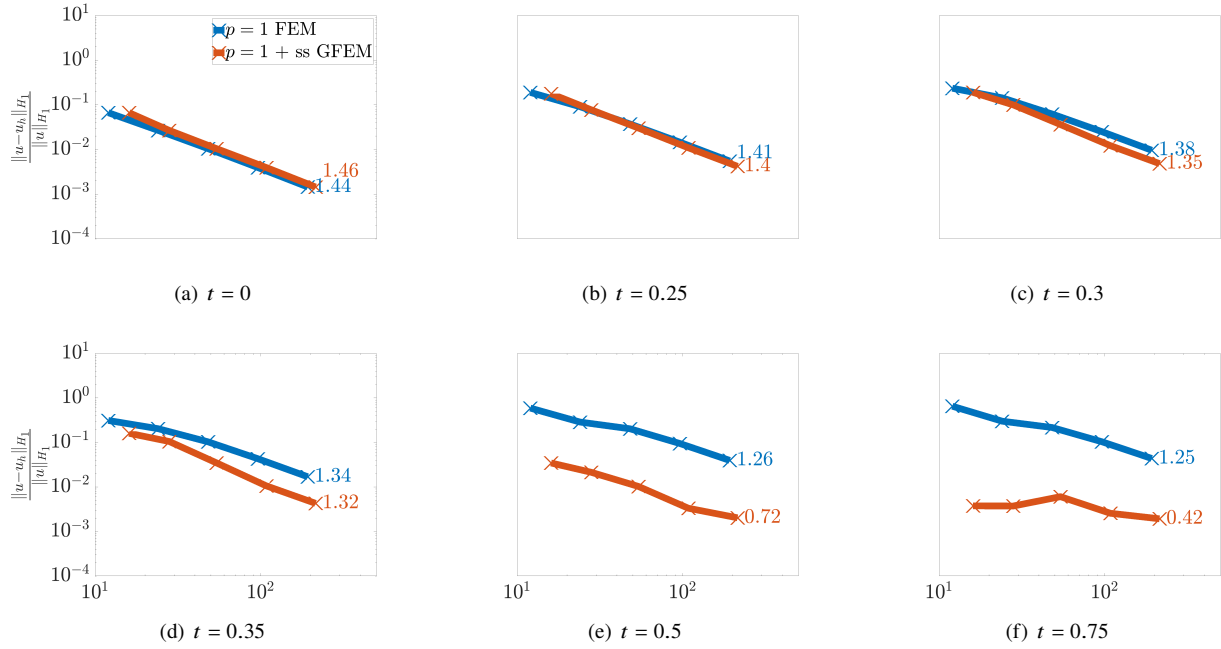


Fig. 27 Convergence the relative H_1 integral norm for the shock problem with $\nu = \frac{1}{100}$

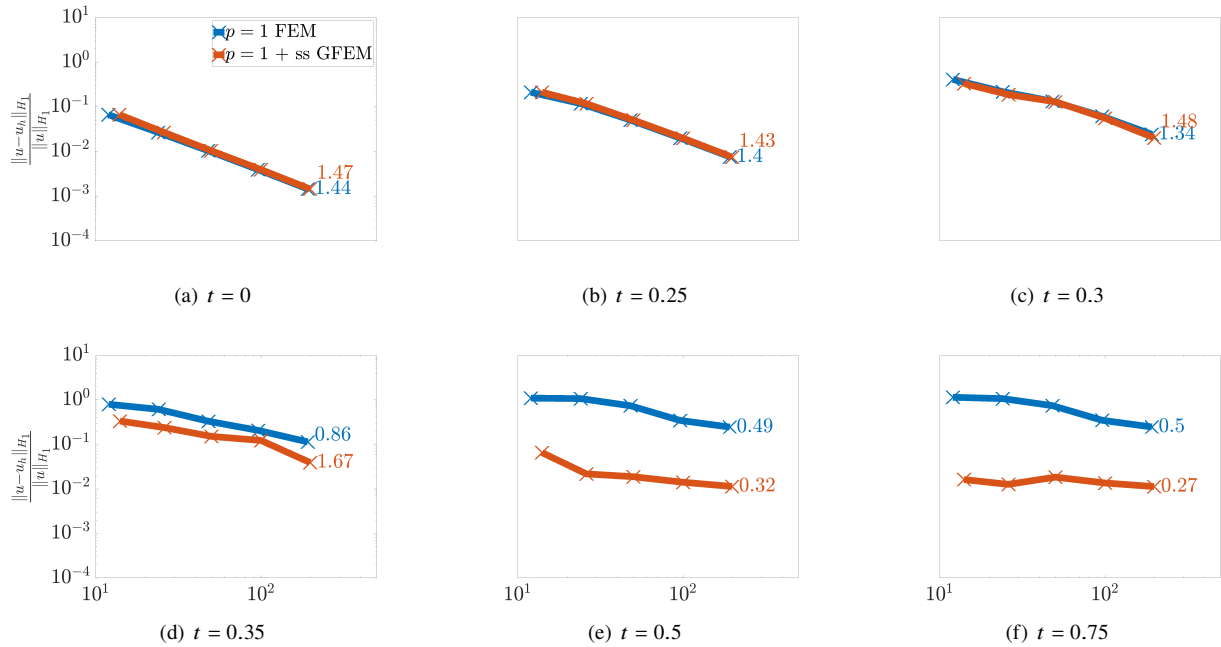


Fig. 28 Convergence the relative H_1 integral norm for the shock problem with $\nu = \frac{1}{500}$

V. Conclusions

This work presents a stable, numerical solution of the one-dimensional, unsteady Burgers' equation for a boundary layer and shock formation problem over a range of small kinematic viscosities. Compared to linear FEM, the GFEM using solution-tailored enrichments yields a significant error reduction at the same number of degrees of freedom. For

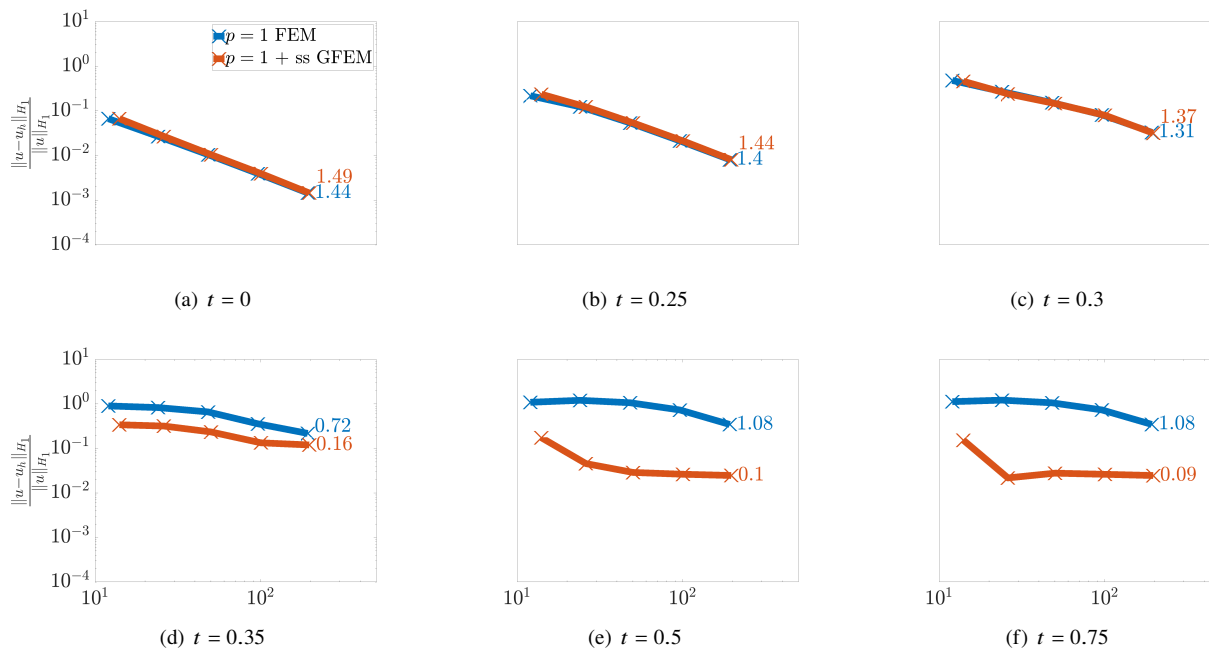


Fig. 29 Convergence the relative H_1 integral norm for the shock problem with $\nu = \frac{1}{1000}$

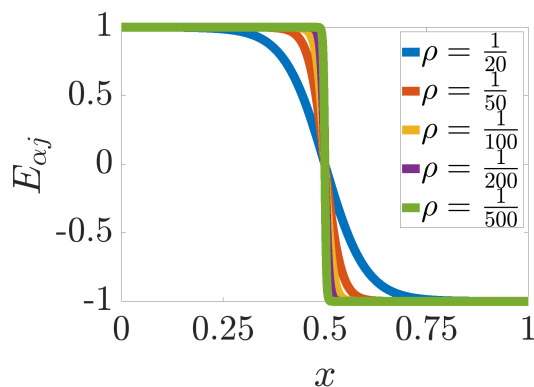


Fig. 30 Set of shock enrichments $\left(E_{\alpha j} = \tanh \left[\frac{1}{2\rho} \left(\frac{1}{2} - x \right) \right] \right)$ for various ρ

the boundary layer problem, the exponential enrichments obtained in [8] are sufficient for capturing the formation of steep boundary layers. For the shock formation problem, hyperbolic tangent functions capture the thin shock forming in the domain. For both examples presented, the enrichments effectively capture the local phenomena up to relatively small kinematic viscosities and reduce errors significantly regarding linear FEM in both the relative L_2 and H_1 norms. However, as the kinematic viscosity approaches extremely small values, the intermediate solution features impact the GFEM solution stability. Specifically, the boundary layer and shock formation in both examples exhibit a range of steep gradients over intermediate time scales when $\nu \ll 1$, which neither the linear interpolation nor initially presented solution-tailored enrichments are sufficient at capturing. The result is spurious oscillations in the GFEM solution during the formation of the boundary layer/shock. These oscillations propagate through later time steps and affect H_1 and L_2 norm convergence. Although oscillations exist in the GFEM solutions over extremely small kinematic viscosities, the oscillations are small over coarse grids, and the errors of the GFEM solutions are still significantly reduced compared to the linear FEM. However, to further improve the shock formation problem results, a set of shock enrichments were introduced to capture the range of scales, resulting in a further reduction of error in both the L_2 and H_1

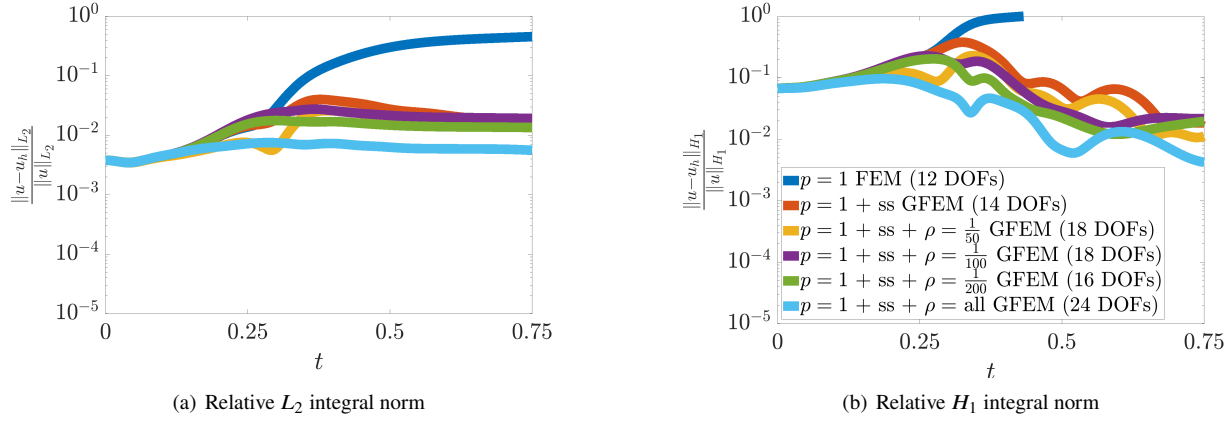


Fig. 31 Relative L_2 and H_1 integral norms versus time for 11-element FEM and GFEM solutions to the shock formation problem when $\nu = \frac{1}{500}$

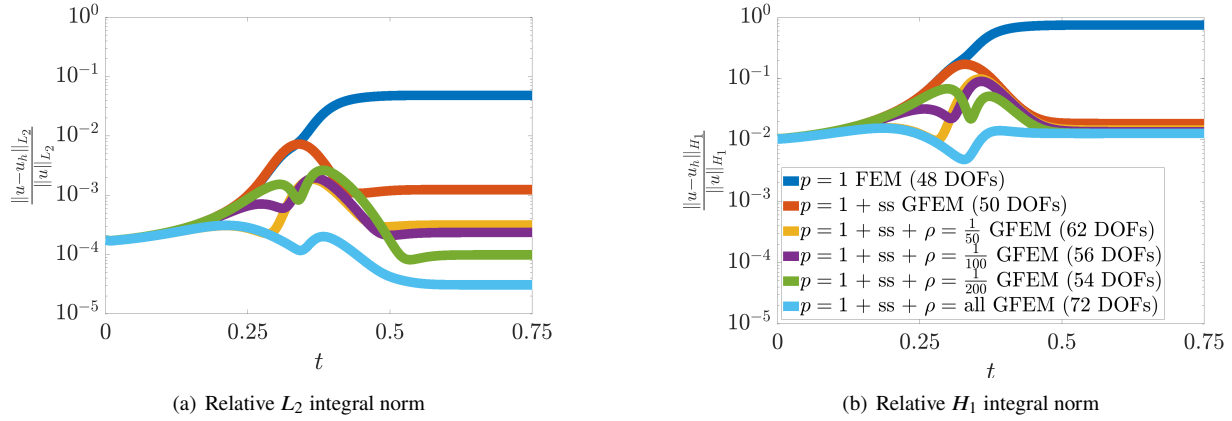


Fig. 32 Relative L_2 and H_1 integral norms versus time for 47-element FEM and GFEM solutions to the shock formation problem when $\nu = \frac{1}{500}$

norms. Specifically, roughly greater than 100 times error reduction is observed compared to the linear FEM at the same number of degrees of freedom. Capturing the intermediate, transitional solution features will likely be an important challenge for solving more complex flow field problems using the presented GFEM framework. Such problems may demand a set of enrichments that capture various scales of the flow as presented in the shock example or time-dependent enrichments as presented in [21]. This analysis is beyond the scope of the current work and a subject for future studies.

Acknowledgments

This work is made possible through an Ohio State Presidential Fellowship to Troy Shilt. The authors thank Prof. C. Armando Duarte, University of Illinois Urbana-Champaign, and Dr. Rohit Deshmukh, The Ohio State University, for their insights on the GFEM.

References

- [1] Oden, J., Duarte, C., and Zienkiewicz, O., "A new cloud-based hp finite element method," *Computer Methods in Applied Mechanics and Engineering*, Vol. 153, No. 1, 1998, p. 117–126. doi:10.1016/S0045-7825(97)00039-X.
- [2] Duarte, C., Babuška, I., and Oden, J., "Generalized finite element methods for three-dimensional structural mechanics problems," *Computers*

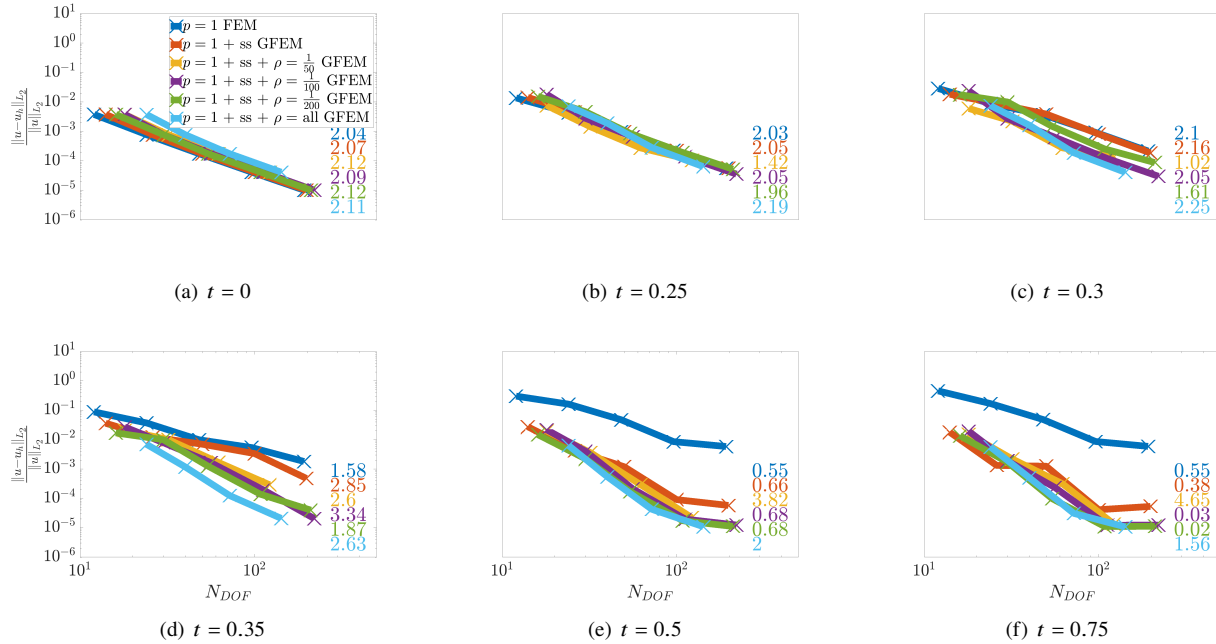


Fig. 33 Convergence the relative L_2 integral norm for the shock problem with $\nu = \frac{1}{500}$

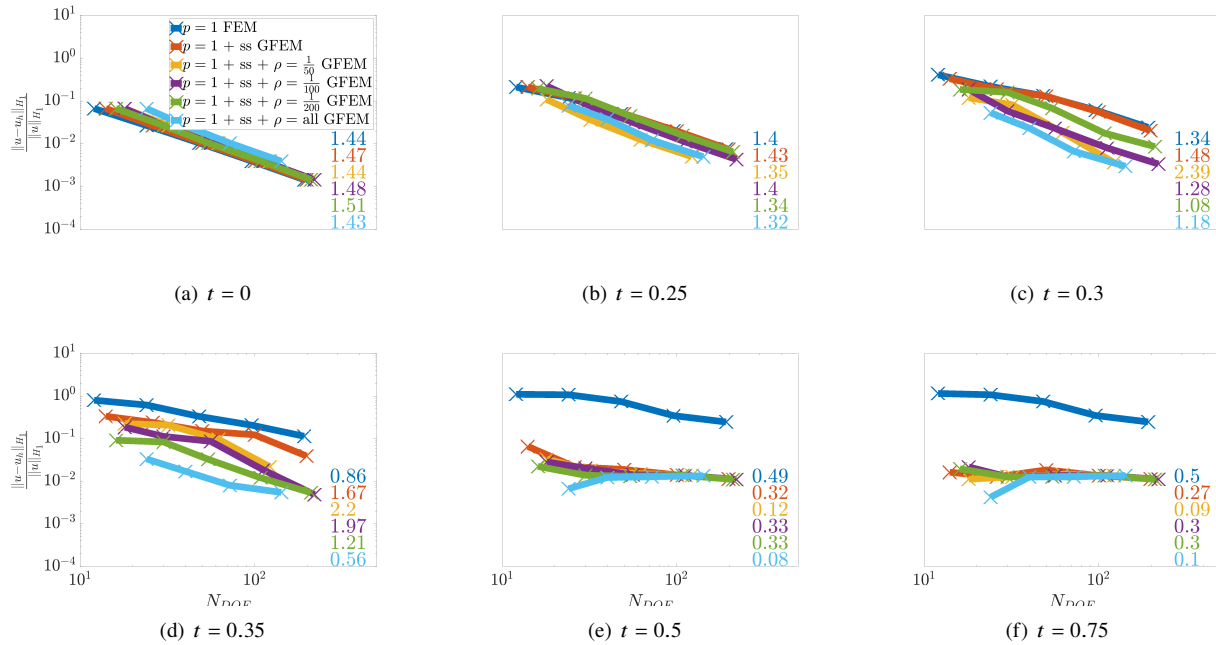


Fig. 34 Convergence the relative H_1 integral norm for the shock problem with $\nu = \frac{1}{500}$

& Structures, Vol. 77, No. 2, 2000, pp. 215–232. doi:10.1016/S0045-7949(99)00211-4, URL <http://www.sciencedirect.com/science/article/pii/S0045794999002114>.

[3] Melenk, J., and Babuška, I., “The partition of unity finite element method: Basic theory and applications,” *Computer Methods in Applied Mechanics and Engineering*, Vol. 139, No. 1, 1996, pp. 289–314. doi:10.1016/S0045-7825(96)01087-0.

- [4] Strouboulis, T., Babuška, I., and Copps, K., “The design and analysis of the Generalized Finite Element Method,” *Computer Methods in Applied Mechanics and Engineering*, Vol. 181, No. 1, 2000, pp. 43–69. doi:10.1016/S0045-7825(99)00072-9.
- [5] Deshmukh, R., Shilt, T., and McNamara, J. J., “Efficient representation of turbulent flows using data-enriched finite elements,” *International Journal for Numerical Methods in Engineering*, Vol. 121, No. 15, 2020, pp. 3397–3416. doi:10.1002/nme.6364, URL <https://onlinelibrary.wiley.com/doi/abs/10.1002/nme.6364>.
- [6] Belytschko, T., Gracie, R., and Ventura, G., “A Review of Extended/Generalized Finite Element Methods for Material Modelling,” *Modelling and Simulation in Materials Science and Engineering*, Vol. 17, 2009, p. 043001. doi:10.1088/0965-0393/17/4/043001.
- [7] Shilt, T., O’Hara, P. J., Deshmukh, R., and McNamara, J. J., “Solution of nearly incompressible field problems using a generalized finite element approach,” *Computer Methods in Applied Mechanics and Engineering*, Vol. 368, 2020, p. 113165. doi:10.1016/j.cma.2020.113165, URL <https://www.sciencedirect.com/science/article/pii/S0045782520303509>.
- [8] Shilt, T., O’Hara, P. J., and McNamara, J. J., “Stabilization of advection dominated problems through a generalized finite element method,” *Computer Methods in Applied Mechanics and Engineering*, Vol. 383, 2021, p. 113889. doi:10.1016/j.cma.2021.113889, URL <https://www.sciencedirect.com/science/article/pii/S0045782521002267>.
- [9] Brooks, A., and Hughes, T., “Streamline upwind/Petrov-Galerkin formulations for convection dominated flows with particular emphasis on the incompressible Navier-Stokes equations,” *Computer Methods in Applied Mechanics and Engineering*, Vol. 32, No. 1-3, 1982, pp. 199–259. doi:10.1016/0045-7825(82)90071-8.
- [10] Hughes, T. J., Franca, L. P., and Hulbert, G. M., “A new finite element formulation for computational fluid dynamics: VIII. The galerkin/least-squares method for advective-diffusive equations,” *Computer Methods in Applied Mechanics and Engineering*, Vol. 73, No. 2, 1989, pp. 173–189. doi:10.1016/0045-7825(89)90111-4, URL <http://www.sciencedirect.com/science/article/pii/0045782589901114>.
- [11] Franca, L. P., and Carmo, E. G. D. D., “The Galerkin gradient least-squares method,” *Computer Methods in Applied Mechanics and Engineering*, Vol. 74, No. 1, 1989, pp. 41–54. doi:10.1016/0045-7825(89)90085-6, URL <http://www.sciencedirect.com/science/article/pii/0045782589900856>.
- [12] Baiocchi, C., Brezzi, F., and Franca, L. P., “Virtual bubbles and Galerkin-least-squares type methods (Ga.L.S.),” *Computer Methods in Applied Mechanics and Engineering*, Vol. 105, No. 1, 1993, pp. 125–141. doi:10.1016/0045-7825(93)90119-I, URL <http://www.sciencedirect.com/science/article/pii/004578259390119I>.
- [13] Franca, L., and Russo, A., “Deriving upwinding, mass lumping and selective reduced integration by residual-free bubbles,” *Applied Mathematics Letters*, Vol. 9, No. 5, 1996, pp. 83–88. doi:10.1016/0893-9659(96)00078-X, URL <http://www.sciencedirect.com/science/article/pii/089396599600078X>.
- [14] BATEMAN, H., “SOME RECENT RESEARCHES ON THE MOTION OF FLUIDS,” *Monthly Weather Review*, Vol. 43, No. 4, 1915, pp. 163–170. doi:10.1175/1520-0493(1915)43<163:SRROTM>2.0.CO;2, URL [https://doi.org/10.1175/1520-0493\(1915\)43<163:SRROTM>2.0.CO;2](https://doi.org/10.1175/1520-0493(1915)43<163:SRROTM>2.0.CO;2).
- [15] Burgers, J., “A Mathematical Model Illustrating the Theory of Turbulence,” Elsevier, 1948, pp. 171–199. doi:10.1016/S0065-2156(08)70100-5, URL <http://www.sciencedirect.com/science/article/pii/S0065215608701005>.
- [16] Bonkile Mayur P., Awasthi Ashish, Lakshmi C., Mukundan Vijitha, and Aswin V. S., “A systematic literature review of Burgers’ equation with recent advances,” *Pramana*, Vol. 90, No. 6, 2018, p. 69. doi:<https://doi.org/10.1007/s12043-018-1559-4>.
- [17] Burgers, J., *The Nonlinear Diffusion Equation*, Springer Netherlands, 1974.
- [18] Bayona, C., Baiges, J., and Codina, R., “Variational multiscale approximation of the one-dimensional forced Burgers equation: The role of orthogonal subgrid scales in turbulence modeling,” *International Journal for Numerical Methods in Fluids*, Vol. 86, 2017. doi:10.1002/fld.4420.
- [19] Gupta, V., Duarte, C., Babuška, I., and Banerjee, U., “A stable and optimally convergent generalized FEM (SGFEM) for linear elastic fracture mechanics,” *Computer Methods in Applied Mechanics and Engineering*, Vol. 266, 2013, p. 23–39. doi:10.1016/j.cma.2013.07.010, URL <http://www.sciencedirect.com/science/article/pii/S0045782513001801>.
- [20] LeVeque, J. R., *Numerical Methods for Conservation Laws*, Birkhäuser Basel, 1992.
- [21] O’Hara, P., Duarte, C., and Eason, T., “Transient analysis of sharp thermal gradients using coarse finite element meshes,” *Computer Methods in Applied Mechanics and Engineering*, Vol. 200, No. 5, 2011, p. 812–829. doi:10.1016/j.cma.2010.10.005.
- [22] Belytschko, T., Moës, N., Usui, S., and Parimi, C., “Arbitrary discontinuities in finite elements,” *International Journal for Numerical Methods in Engineering*, Vol. 50, No. 4, 2001, p. 993–1013. doi:10.1002/1097-0207(20010210)50:43.0.CO;2-M, URL [https://onlinelibrary.wiley.com/doi/abs/10.1002/1097-0207\(20010210\)50:43.0.CO;2-M](https://onlinelibrary.wiley.com/doi/abs/10.1002/1097-0207%2820010210%2950%3A4%3C993%3A%3AAID-NME164%3E3.0.CO%3B2-M).
- [23] Kutluay, S., Bahadır, A., and Özdeş, A., “Numerical solution of one-dimensional Burgers equation: explicit and exact-explicit finite difference methods,” *Journal of Computational and Applied Mathematics*, Vol. 103, No. 2, 1999, pp. 251–261. doi:10.1016/S0377-0427(98)00261-1, URL <http://www.sciencedirect.com/science/article/pii/S0377042798002611>.
- [24] Dey, S. K., Dey, C., and Center, A. R., *An explicit predictor-corrector solver with applications to Burgers’ equation [microform] / Suhrit K. Dey and Charlie Dey*, National Aeronautics and Space Administration, Ames Research Center Moffett Field, Calif, 1983.
- [25] Ozis, T., and Ozdes, A., “A direct variational methods applied to Burgers’ equation,” *Journal of Computational and Applied Mathematics*, Vol. 71, No. 2, 1996, pp. 163–175. doi:10.1016/0377-0427(95)00221-9, URL <https://www.sciencedirect.com/science/article/pii/0377042795002219>.